Title: Cortical microtubules act as a template to organize nano-scale patterning of exocytosis

Authors: Jelmer J. Lindeboom[1,2]*, Ryan Gutierrez[1,3], Viktor Kirik[4] and David W. Ehrhardt[1,3]*

Affiliations:

[1]Department of Plant Biology, Carnegie Institution for Science; Stanford, CA 94305, USA.

[2]Current Address: Novo Nordisk Foundation Center for Genomic Mechanism of Disease, Broad Institute of MIT and Harvard, MA 02142, USA.

[3]Department of Biology, Stanford University; Stanford, CA 94305, USA.

[4]School of Biological Sciences, Illinois State University; Normal, IL 61790, USA.

*Corresponding authors

Email: ehrhardt@stanford.edu

jelmer@broadinstitute.org

Abstract

The microtubule cytoskeleton plays an important role in targeting and organizing exocytosis, enabling cellular morphogenesis, motility and polarized transport. However, in many organisms and cell types, the mechanisms by it does so are not well understood. Here, we identify the exocytotic protein KEULE, an essential SEC/MUNC, as a dynamic marker for exocytosis that forms clusters that are associated with and required for discrete exocytotic events in growing *Arabidopsis* cells. Live cell imaging revealed that these clusters, including those associated with verified exocytotic events, have stereotyped and distinct patterns of protein accumulate and loss, suggesting discreet phases in the assembly, function and of exocytotic protein complexes. Super-resolution image analysis revealed that exocytotic events marked by these KEULE clusters are not randomly distributed at the plasma membrane but are significantly enriched in ~180 nm wide linear domains that flank cortical microtubules associated with the plasma membrane, while being under-represented in adjacent domains ~520 nm wide. Thus, the cortical microtubule array acts as a highly organized and dynamic two-dimensional template that effectively redistributes and patterns a significant portion of exocytotic traffic. This positioning mechanism differs from previously reported mechanisms based on directed transport to microtubule ends, allowing for linear and ordered deposition of cargoes to the cell membrane and extracellular matrix to support functions such as cell morphogenesis. The role microtubule arrays near or at the plasma membrane play in organizing exocytosis may be conserved in other cell types and organisms.

Significance Statement

Cells deliver transmembrane proteins and extracellular matrix material through exocytosis, the process of vesicular fusion to the plasma membrane. The plasma membrane contains specialized subdomains crucial for cell shape and function, requiring precise spatial control over exocytosis. Microtubules organize exocytosis partly by transporting vesicles from the cell body to the periphery along oriented centrosomal arrays, but how acentrosomal microtubule arrays organize exocytosis remains poorly understood. We found that in plant cells, which completely lack centrosomes, microtubules define linear and highly structured plasma membrane domains of increased and decreased activity of individual exocytotic events. This demonstrates a means by which ordered microtubule organization may generate functional anisotropy crucial for morphogenesis in plant cells, a mechanism possibly shared by other acentrosomal arrays.

Main Text

Introduction

The ability to organize biomolecules at the cell cortex was a fundamental innovation in the evolution of cellular life, enabling essential biological functions including cellular morphogenesis, motility and polarized transport. Targeted exocytosis, non-random positioning and fusion of exocytotic vesicles at the plasma membrane, is a crucial mechanism for creating such cortical organization. Across phyla, the actin and microtubule cytoskeletons have been implicated in spatial organization of exocytosis. This functionality is exemplified in plant and fungal cells by cellular tip growth, and in animal cells by polarization of mammalian epithelia, cell migration and the positioning of focal adhesions[1,2]. The molecular polarity of microtubules plays an important role in how their function in exocytotic targeting is understood. For example, polarized arrays of microtubules created by nucleation from centralized organizing bodies - such as centrosomes or Golgi - can serve as directional tracks for motor-driven transport of exocytotic vesicles from where they are created in the cell interior to peripheral destinations at the plasma membrane[2,3]. More refined positioning of exocytosis is proposed to be accomplished by association of microtubule plus ends with specific locations at the plasma membrane, including focal adhesions[2]. Polarized arrays of microtubules can also organize exocytosis through directed transport of

factors that establish membrane domains that serve to target exocytotic traffic, as exemplified during tip growth in fission yeast[4]. However, many cells across diverse organisms feature interphase microtubule arrays that are not centrally organized and have architectures where microtubules are not clearly polarized with respect to the plasma membrane[5]. Acentrosomal arrays are required in important biological processes that require exocytosis, such as morphogenesis, but relatively little is understood about how they may function to target and pattern exocytotic traffic.

Gaining an understanding of exocytotic targeting mechanisms requires an ability to observe individual exocytotic events with respect to targeting machineries and a means to verify successful delivery of exocytotic cargo. Observing individual exocytosis events has been challenging in many cell models because microtubules, exocytotic vesicles and the machineries of exocytosis are often densely concentrated. Axially growing cells in the epidermis of higher plants have features that provide an excellent experimental platform to make such observations and for investigating how acentrosomal microtubule arrays may target and pattern exocytosis. In contrast to cells with microtubule arrays that are polarized with respect to the cell interior and the plasma membrane, these cells feature highly ordered arrays of microtubules that lie at the cell cortex in parallel to and in contact with the plasma membrane along their lattices. Large regions of the plasma membrane lie in a single focal plane, where the individual microtubules and microtubule bundles that constitute these arrays are easily visualized due to their quasi-2-dimensional nature and comparatively low density[6]. In previous studies, we determined that cellulose synthase complexes (CSCs), large integral membrane protein complexes that synthesize and extrude cellulose into the cell wall, can be used to observe individual exocytotic events at the plasma membrane by allowing dynamic tracking of both exocytotic vesicles and the successful delivery of cargo to the plasma membrane[7–9]. By tracking CSCs while simultaneously imaging dynamic cortical arrays, we discovered that CSCs were preferentially delivered to the plasma membrane at locations defined by microtubules. This targeting did not involve vesicular transport along microtubules, nor did it involve defining exocytotic domains by end-on association of microtubule ends with the plasma membrane[7], thus suggesting a previously undescribed mechanism for microtubule-dependent exocytotic targeting. However, CSC's themselves have been shown to interact with microtubules via a specific protein, Cellulose Synthase-Interaction 1 (CSI1), an interaction that can also tether CSC-containing vesicles and organelles to microtubules[10–13]. Thus, it was not clear if this exocytotic patterning mechanism may be widely employed in plant cells, or if it is unique to delivery of CSCs to the plasma membrane.

Microtubule targeting of exocytosis is of special interest in the context of plant cell morphogenesis because ordered cortical microtubule arrays are essential to create functional cell shape. Depolymerization of microtubules by the drug oryzalin causes isotropic growth and a complete loss of genetically determined cell shape. The predominant hypothesis for the function of cortical microtubules in directing cell growth is that they guide and organize the trajectories of CSCs as they synthesize and extrude cellulose microfibrils into the cell wall, thus creating material and mechanical anisotropy that directs expansion of the cell wall (which is under tension generated by high turgor pressure). We confirmed that individual CSC trajectories are in fact guided by microtubules by live cell imaging studies[14]. However, disruption of both microtubule guidance of CSCs and delivery of CSCs to the plasma membrane in *csi1* null mutants causes only a modest loss of cell growth anisotropy[10,11,13]. In addition, although complete loss of growth anisotropy is caused by microtubule depolymerization, this phenotype is not due to a loss of CSC delivery to the plasma membrane[7] nor a lack of ordering in CSC trajectories[7,15,16]. Further, cell growth rate does not appear to be impaired by oryzalin treatment and loss of cortical microtubules[17]. These observations suggest that cortical microtubules arrays have additional important functions in establishing cell shape, prompting us to ask if cortical microtubules may guide cellular morphogenesis by acting as a general targeting mechanism, beyond CSC's, to pattern exocytosis during cell growth.

To determine if individual exocytosis events in growing plant cells are broadly patterned by cortical microtubule targeting, we require a dynamic biological marker that identifies single exocytotic

113 events and is involved in a wide range of exocytotic traffic to the plasma membrane. To date, such a
114 marker has not been identified. Imaging studies of core exocytotic proteins, including soluble *N*-
115 ethylmaleimide-sensitive factor attachment protein receptors (SNARE proteins)[18–20] and components of
116 the exocyst complex[21,22], have not revealed a clear relationship between the presence and dynamics of
117 these proteins with verified exocytosis events nor have they shown association of these proteins with
118 microtubules[23].

119 To address this gap in tools for studying individual exocytotic events, we investigated use of the
120 essential Sec/Munc (SM) protein KEULE. SM proteins are essential regulators of SNARE-mediated
121 vesicle fusion. In exocytosis, SNARE proteins anchored to the vesicle interact with those on the plasma
122 membrane and form a membrane bridging complex with other partners that enables membrane fusion[23–25].
123 The soluble SM proteins are known to bind to SNAREs, and evidence from genetic studies together with
124 *in vivo* and *in vitro* experiments suggest they function in vesicle docking, SNARE complex assembly and
125 vesicle fusion[26–31]. In plants, the *Arabidopsis* Sec1 homolog KEULE was identified in a genetic screen for
126 embryonic pattern mutants[32], where loss of function mutations are lethal, causing bloated and
127 multinucleate cells[33]. Consistent with other SM proteins, KEULE interacts genetically and biochemically
128 with Qa-SNAREs, specifically KNOLLE (SYP111) and SYP121, and has been shown to play essential
129 roles in cell plate assembly during cytokinesis and exocytotic traffic to the plasma membrane[18,33–37]. The
130 demonstrated function of KEULE in exocytosis, combined with its severe loss of function phenotype due
131 to lack of exocytosis suggested that KEULE might serve as an excellent candidate for a generalized
132 reporter of exocytosis.

133 The molecular and structural mechanisms by which SM proteins interact with and regulate
134 SNARE complex assembly have been investigated intensively by genetic, biochemical, *in vitro* and
135 structural studies[26–31], and SM proteins have been imaged in live cells in several systems[38–45]. However,
136 important features of their behaviors and biological function in living cells remain to be uncovered. These
137 questions include the fine scale cellular distributions of SM proteins and clusters, the association of SM
138 clusters with exocytosis events, the relationship of these exocytosis events to potential organizing
139 machineries and the dynamics of SM assembly and loss at exocytosis sites, especially prior to and during
140 vesicle fusion.

141 Here, we develop and apply automated and high precision analysis methods to detect and track
142 tens of thousands of individual and fluorescently tagged KEULE clusters to investigate their dynamics
143 and to map their positions at the plasma membrane in living cells. We evaluate these clusters as
144 exocytotic events by use of CSCs as a validated cargo and employ genetic analysis to test for the function
145 of KEULE in CSC delivery. Finally, we use high precision mapping of KEULE clusters and
146 microtubules, combined with Bayesian methods, to quantitatively determine if the cortical microtubule
147 cytoskeleton as a template in patterning exocytosis.

148 **Results**

149

150 **Functional dynamics of tdTomato-KEULE cluster formation**

151 To visualize KEULE protein *in vivo*, we created a tdTomato-KEULE fluorescent reporter
152 constructed from the chromosomal gene with native upstream regulatory sequence and introduced it into
153 *Arabidopsis* plants heterozygous for a *keule* deletion allele. To obtain plants for study of KEULE
154 localization and dynamics, we screened for self-fertilized progeny of these transgenic plants that exhibited
155 rescue of *keule* loss of function phenotype by the tagged KEULE protein. These plants exhibited full
156 rescue of plant growth and development through the 5-day seedling stage used for our further studies
157 (Fig. S1, Methods).

158 In dark-grown *Arabidopsis* hypocotyl cells expressing the tdTomato-KEULE construct, we
159 observed KEULE signal appear as densely distributed and temporally dynamic puncta at the plasma
160 membrane (Fig. 1A). The dynamics of signal increase and decay were apparent in time-lapse movies

(Movie S1), kymographs of signal intensity over time along transect lines (Fig. 1B) and in sequential image samples of individual puncta (Fig. 1C). In all these events, a steady increase in signal intensity was observed, followed by an abrupt decrease and disappearance of signal. This behavior indicates the accumulation and loss of many fluorescently labeled KEULE proteins, which we will refer to hereafter as clusters.

The dynamics of tdTomato-KEULE accumulation and disappearance are presumably related to its function. Therefore, we reasoned that a quantitative and robust picture of KEULE cluster dynamics would be useful in gaining insight into the underlying molecular mechanisms of exocytosis. To accomplish this, we collected a large-scale and high-resolution dataset comprising thousands of individual events. We acquired streamed images at 200 ms intervals and performed automated detection and frame-to-frame linking of KEULE cluster signal using μTrack[46]. These track data were then used to extract position and intensity information by Maximum Likelihood Estimate 2D Gaussian fitting[47] (see Methods, Movie S2). To define events of signal appearance, accumulation and loss, we used a minimum sample of 4 sequential acquisitions, which made our shortest measured lifetimes approximately 800 ms. The lifetime distribution of tdTomato-KEULE clusters showed a large range, from this minimal event length of 800 ms to over half a minute. These data followed a roughly exponential distribution with a mean of 2.34 s and ~95% of lifetimes being less than 7 seconds long (Fig. 1D).

The large lifetime range of observed KEULE cluster events might represent a collection of functional classes. If so, such classes may by differentiated by their kinetics. To assess the kinetics of KEULE signal accumulation and loss, and to ask if these kinetics might vary as a function of cluster lifetime, we leveraged our large data set to calculate KEULE kinetics for each 200 ms lifetime increment. Fig. 1E shows average intensities for all observed clusters with lifetimes of 4.2, 4.4 and 4.6 s. All these plots show a similar pattern: an initial steep rise in intensity, followed by a steady increase, then a short plateau phase, and ending with a sharp decrease. When we extended this analysis over a larger range of lifetimes, we observed evidence that the shortest-lived events accumulated tdTomato-KEULE intensity at a slower rate, suggesting they might be a functionally different class (Fig. 1F). At longer lifetimes, the plateau phase became more extended, suggesting that these events may be paused or stalled (Fig. 1F). To quantitatively compare differences in accumulation kinetics as a function of cluster lifetime, we grouped events into three duration classes; short (0.8 to 1.6s), medium (1.8 to 6.2s) and long (6.4+s) – and then averaged the intensities at each 200 msec timepoint (Fig. 1G, for details see Methods). The timepoints following the plateau phase were omitted to aid comparison of signal accumulation trajectories. This analysis confirmed that, indeed, the short events show significantly slower signal accumulation (Fig. 1G). Interestingly, the medium and long cluster lifetimes show nearly identical trends in signal intensity accumulation over time, indicating that they might be part of the same functional population during KEULE recruitment/assembly. It is noteworthy that for events up to ~5s, maximum cluster signal intensity increased with cluster lifetime. A possible explanation for this relationship is that longer accumulation events represent the assembly of exocytotic apparatus at larger vesicles. SEM studies of *in vitro* vesicle fusion, for example, have shown that more SNARE proteins are present at the fusion sites of larger vesicles as compared to smaller vesicles[48,49] In events lasting longer than about 5 seconds maximum signal no longer increased with lifetime but instead showed a prolonged plateau phase, possibly indicating stalled exocytosis events or alternatively, an extended checkpoint.

Clusters of tdTomato-KEULE coincide with CSC delivery to the plasma membrane

To place SM protein accumulation in context of functional exocytosis, we took advantage of our previous work on delivery of CSCs to the plasma membrane[7]. CSCs are assembled in the Golgi system from multiple CESA catalytic subunits[50,51], move through the trans-Golgi network (TGN) and are budded off into vesicles that fuse with the plasma membrane[7]. Because CSCs are formed of multiple CESA subunits, they can be labeled by fluorescent proteins in sufficient number to allow their detection and the

209 tracking of individual complexes during the process of exocytosis. Labeled vesicles display rapid and
210 erratic dynamics that abruptly become stabilized at the optical plane of the plasma membrane with a mean
211 duration of about 60 seconds, followed by a transition to slow, steady and typically linear motility of
212 between 250 and 450 nm/min. The transition erratic to static movement is interpreted as evidence for
213 vesicular capture and tethering at the plasma membrane, and the transition to slow and steady movement
214 indicates successful vesicle fusion and delivery of CSCs, which are propelled by the synthesis and
215 extrusion of cellulose microfibrils[7,14]. This stereotyped behavior makes CSCs an excellent reporter for
216 successful exocytosis, revealing a time and place for vesicle tethering, and distinguishing vesicle tethering
217 at the plasma membrane from successful vesicle fusion and cargo delivery.

218 To visualize KEULE together with CSCs, we generated plants that express tdTomato-KEULE
219 and CIT-CESA6, a catalytic CSC subunit labeled with Citrine fluorescent protein[14] in a *keule*/*cesa6*
220 double mutant background (Methods). CIT-CESA6 signal is relatively dense in the plasma membrane of
221 rapidly growing cells so we photobleached the CIT-CESA6 signal over a region of the plasma membrane
222 to aid detection of new CSC arrivals and their relation to td-Tomato-KEULE signal (Fig. 2A, Movie S3).
223 For each CSC arrival at the optical plane of the plasma membrane, we determined the first frame in which
224 the CESA6 signal became stationary (an indication of interaction and tethering at the plasma membrane).
225 We then identified the nearest KEULE cluster in a range of -10 to 50 seconds of the first stable CESA6
226 frame and determined the distance between the centroid of the CESA6 signal and the centroid of the
227 nearest KEULE signal by maximum likelihood 2D Gaussian fitting (See Methods, Fig. 2B and D). A
228 search range starting at -10 seconds was chosen because the exact frame of stationary transitions was in
229 some cases obscured by signal from clusters of other labeled organelles such as Golgi bodies and TGN. If
230 KEULE is involved in the exocytotic delivery of CSCs to the plasma membrane, we expect to observe co-
231 localization between CSC delivery events and KEULE clusters. However, CSC deliveries, as defined by
232 static tracks, are relatively sparse and long lived as compared to KEULE cluster events, so some degree of
233 colocalization in space and time is expected by chance alone. To assess statistically the spatial and
234 temporal association of CSC delivery events and KEULE clusters, we generated a simulated dataset of
235 random locations within the photobleaching areas and identified the nearest KEULE spot to the random
236 locations within the same time window we used for our experimental observations. We then compared the
237 distributions of distances to the nearest KEULE cluster between the observed CSC deliveries and the
238 simulated data (Fig. 2B) and found that the experimental data were strongly skewed to shorter distances
239 ($p < 1E-06$, Kolmogorov-Smirnov test). The pattern of over- and under-representation of observed with
240 respect to simulated data is more easily seen in a plot of the bin-by bin differences where shorter KEULE-
241 microtubule distances are seen to be over-represented in bins below 200 nm and underrepresented in bins
242 of longer values (Fig. 2C). Using a Bayesian method (See Methods), we found that the most likely values
243 of the experimental biases from the null hypothesis of a random association were significantly above that
244 expected by chance alone for distance bins below 120 nm (Fig 2E and F) and significantly lower than
245 expected in bins of longer distances from 200 to 480 nm. Based on these data we defined colocalization
246 as observing a KEULE cluster centroid within 200 nm from the position of CSC signal in the first frame
247 in which it was observed to stabilize (and in a time window of -10 to 50 seconds around that frame). By
248 these criteria, colocalization occurred in 81% (157 out of 194) of observed delivery events compared to
249 29% (13035 out of 45051) of random locations at the plasma membrane ($p < 1.4E-50$, Fisher's exact test).

250 We considered that our automated experimental protocol may allow for underestimation of
251 colocalization between CSC delivery and KEULE. For example, the time interval used for these
252 experiments is 2.11 s, of which 400 ms is used for tdTomato-KEULE excitation and image acquisition.
253 Since a substantial portion of KEULE cluster lifetimes is shorter than the ~1.7 s gaps between image
254 acquisitions, we do not expect to detect all KEULE clusters within the -10 to 50 second experimental
255 window. In addition, not all excited KEULE foci are successfully identified by the spot detection and
256 filtering routines used for large-scale data collection. To understand how these two cases, no excitation
257 and no detection, affect our colocalization results, we performed a hand-curated analysis using a custom
258 MATLAB GUI. For each CSC delivery, we examined whether there was overlap of KEULE signal with

259 the centroid of the CSC signal in the first frame of positionally stable KEULE signal (tethering frame).
260 We found that in 92% (159 out of 172) of the cases, KEULE signal was observed to overlap the CSC
261 position in the tethering frame within -10 to 50 s of CSC stabilization, suggesting that our automated
262 analysis, while free of possible observer bias, may underestimate the true degree of colocalization
263 frequency of CSC exocytosis events and KEULE.

264 If KEULE clusters function in CSC exocytosis after vesicle tethering, we expect that not only
265 should they colocalize with CSC signal, but that the time intervals between vesicle tethering and the
266 recruitment of KEULE should have a non-random distribution. We tested this prediction by comparing
267 the delay times for arrival of the nearest KEULE spot following the tethering frame in the observed vs the
268 simulated KEULE data sets. The observed delay time distribution was significantly different from the
269 random distribution of the simulated data ($p < 7.8E-04$ Mann-Whitney U test) (Fig. 3A), having a peaked
270 distribution with a median of 2.111 s and a mean of 7.92 s, suggesting that KEULE is recruited and
271 functions within several seconds after the CSC vesicle is stabilized and tethered at the plasma membrane.

272 The durations of KEULE clusters associated with CES deliveries had a distribution similar in
273 character to that observed For KEULE clusters in general (Fig. 3B, compare to Fig.1D), with both
274 appearing roughly exponential but long tailed. While lifetimes of clusters associated with CESA
275 deliveries spanned a similar range of durations, those associated with CESA delivery were observed to
276 have a significant bias towards longer values, with clusters associated with CESA having a median
277 duration of 4.3 seconds, as compared to 2.3 seconds for clusters in general. To test the significant of this
278 observed bias, we compared the relative frequencies of durations longer than two seconds and found a
279 highly significant difference - 59% vs 37% for CESA delivery-associated KEULE clusters events vs
280 clusters in general (Fig. 3C, p=6.07E-09 Fisher's exact test). These results indicate that both short-lived
281 and long-lived KEULE clusters are associated with verified exocytosis events and that those associated
282 with CESA complexes are modestly biased towards longer lifetimes. Taken together, our data now
283 provide insight into the kinetics of SM protein recruitment to sites of exocytosis and reveal the time of
284 vesicle fusion following exocytotic vesicle stabilization and tethering at the plant cell plasma membrane.

285 Our data show that KEULE clusters are associated with confirmed sites of CSC exocytosis in
286 both space and time, but is KEULE function required for CSC exocytosis? To answer this question, we
287 quantified CSC delivery in selfed progeny of parental plants homozygous for a transgene expressing CIT-
288 CESA6, heterozygous for a *tdTomato-KEULE* allele, and homozygous for *cesa6* and *keule* loss of
289 function alleles (See Methods). Seedlings tested for loss of KEULE function were identified by
290 morphological *keule* phenotype (severely reduced in size, large and misshaped cells) and little to no
291 tdTomato-KEULE signal. In these mutant seedlings, we found that the CSC delivery rate was reduced by
292 over 17-fold as compared to that in wildtype ($p<0.0001$, Wilcoxon two sample test, Fig. 2G). Taken
293 together our results indicate that KEULE plays an essential role in plasma membrane delivery of primary
294 CSCs, and that CSC delivery is spatially and temporally associated with KEULE clusters which display
295 stereotyped dynamics of formation and loss.

296 **KEULE dynamics are sensitive to drugs and treatments that reduce exocytosis**

297 We previously reported that the number of active CSCs in the plasma membrane were rapidly and
298 significantly reduced by treatment with mannitol (osmotic stress) and the herbicide isoxaben[7].
299 Measurements of CSC delivery revealed that mannitol treatment also caused a 100-fold reduction in the
300 delivery rate of CSC's, indicating that CSC loss at the plasma membrane was likely caused primarily by
301 inhibition of exocytosis. Likewise, isoxaben has been characterized as a specific cellulose synthase
302 complex inhibitor[52], but its mode of action is also not well understood. Here we (1) determine if isoxaben
303 treatment also reduces CSC exocytosis and (2) ask if KEULE dynamics may provide insight into how
304 osmotic stress and isoxaben act to inhibit exocytosis.

305 To address the above questions, we treated seedlings expressing tdTomato-KEULE and Cit-
306 CESA6 with either 200 mM mannitol, 100nM isoxaben or carrier only (0.01% DMSO, mock) and

307 assayed CSC delivery to the plasma membrane as described above. We found that, like osmotic stress
308 caused by mannitol, isoxaben is also a potent inhibitor of CSC exocytosis, reducing CSC delivery rate by
309 ~70 fold (Fig. S2). By contrast to CSC delivery, the overall frequencies of KEULE cluster formation after
310 both mannitol and isoxaben treatment were not significantly lower than that observed for mock treatment,
311 indicating that neither acts to absolutely block initial KEULE recruitment and cluster formation rates (Fig.
312 S3A). However, when we examined KEULE accumulation dynamics we observed striking differences
313 among treatments (Fig. S3B, C). In cells treated with mannitol KEULE signal accumulated more slowly
314 and to lower levels in the short and intermediate lifetime classes events (Fig. S3B). Intriguingly, the
315 trajectories of long duration clusters (6.4 s or longer) exhibited a markedly different pattern. KEULE
316 signal trajectories for both mock and mannitol treated cells tracked each other closely for the first 5 s or
317 so, but rather than reaching a plateau after 5 seconds, signal in mannitol treated cells continued to increase
318 steadily until the transition to rapid signal loss (Fig. S3B). Taken together, these data suggest that there
319 may be two different mechanisms by which mannitol treatment and osmotic stress affects KEULE
320 dynamics, depending on their duration class: one mechanism that acts negatively and from cluster
321 inception that reduces the rate and level of KEULE accumulation in short and intermediate events, and
322 one which acts at a later stage in long duration events that prevents transition to the normally occurring
323 plateau stage. By contrast, we observed that isoxaben treatment slowed accumulation of tdTomato-
324 KEULE across events of all durations (Fig. S3C).

325 We observed related differences among treatments in KEULE cluster lifetimes. In comparing the
326 distributions of cluster lifetimes in mock and mannitol treated cells, a bimodal effect was again observed,
327 with both shorter and longer lifetimes being over-represented in comparison with mock treatment (and
328 intermediate events being under-represented) (Fig S4A, B, D). As was the case with intensity dynamics,
329 isoxaben treatment showed more of a unimodal effect, with the lifetime distribution being shifted to the
330 left (Fig. S4B, C, E). Mannitol and isoxaben also caused diverging effects on persistence of KEULE
331 clusters, as assessed by survival analysis (Fig. S4F, G). Taken together, our data show that KEULE
332 cluster dynamics are sensitive to perturbations that affect exocytosis and reveal evidence that mannitol
333 and isoxaben treatments affect these dynamics in distinct ways, suggesting they may perturb exocytosis
334 by different mechanisms.

335

336 **Cortical microtubules pattern KEULE cluster distribution and exocytosis**

337 Having established dynamic KEULE clusters as markers of exocytotic events, we noted that the
338 flux of KEULE cluster formation, 144 events per μm^2 per h (Fig. S3A), is ~85-fold higher than that of
339 CSC delivery (1.59 evens per µm2 per h, Fig. 2G). We therefore utilized dynamic imaging of KEULE
340 and microtubules together to ask if cortical microtubules pattern the distribution of KEULE protein and to
341 determine if targeting of exocytosis is specific for CSCs or if it is a broad and fundamental function for
342 the cortical microtubule cytoskeleton in growing plant cells. Further, we took advantage of the ability to
343 detect thousands of KEULE clusters to map the spatial range of influence of microtubule targeting with
344 super-resolved precision.

345 To visualize KEULE cluster events together with cortical microtubules, we performed live cell
346 imaging at 1 second intervals in hypocotyl cells of *Arabidopsis* seedlings expressing GFP-TUA5 and
347 tdTomato-KEULE in a *keule* knock-out background (Fig. 4A, Movie S4). We tracked individual KEULE
348 events at the plasma membrane and used MLEwG fitting to extract precise positional information (Fig.
349 4B, Methods), after which we identified the frame with peak signal intensity as the reference point for
350 each detected KEULE cluster position (Fig. 4C panels 1-3). We then measured signal intensity in the
351 microtubule channel along a series of scan lines that were rotated at 9° intervals around the centroid of the
352 KEULE cluster (Methods and Fig. 4C panel 4). On each of these scan lines, we detected all microtubule
353 signal peaks and fit them with a modified quasi-1-dimensional MLEwG fit (Methods, Fig. 4D). Since the
354 microtubule signal is best represented as a quasi-1-dimenional Gaussian orthogonal to the microtubule

355 axis, we determined the orientation of the nearest microtubule as identified by peak analysis and used the
356 scan line most orthogonal to the microtubule angle for determining the location of the microtubule central
357 axis closest to the KEULE spot in question (Fig. 4C, panel 5). For example, the intensity of KEULE
358 signal in photoelectrons for the most orthogonal scan line in Fig. 4C panel 5 is shown in Fig. 4D panel 1,
359 the triple Gaussian 1D MLEwG fit in panel 2, and the decomposed individual peak fits in panel 3. We
360 used the fit positional coordinates of the nearest microtubule signal peak and the KEULE cluster to
361 calculate the distance and the photoelectron fit values to estimate the standard error of the measurement
362 (See Methods and Fig. 4C panel 6). We repeated this process for all detected KEULE tracks in each
363 movie to assess the spatial relationship between KEULE clusters and the nearest microtubules to those
364 clusters (Fig. 4E, panel 1).

365 To ask if the measured distribution of KEULE to microtubule distances differs from that expected
366 if KEULE cluster positions are independent of microtubule locations (the null hypothesis), we first
367 needed to determine what the expected distributions are under the null hypothesis when our detection and
368 analysis routines are applied to the image datasets we used for our experimental observations. For
369 example, microtubule array structure, which varies within and among cells, will have a strong influence
370 on this distribution, as will the dimensions of our detection kernels. Therefore, we generated a simulated
371 set of random locations within each region of interest across all image frames in the movies and
372 calculated the distances from these synthetic KEULE foci to the nearest microtubule (Fig. 4E, panel 2).
373 When the experimental and expected distributions were plotted together as relative frequencies, they
374 showed evidence for distinct differences (Fig. 5A). The spatial pattern of under- and over-representation
375 is more easily visualized in a plot of the differences between observed and expected frequencies (Fig.
376 5B). To quantify over- or under-representation of the experimental data given the expected data under the
377 null hypotheses, we used a Bayesian method to determine the most likely positive or negative bias at each
378 distance bin (Fig. 5C and D and Methods). We found that at KEULE-microtubule distances smaller than
379 180 nm, the maximum likelihood bias was significantly positive (more frequent than expected) and
380 between 180 and 700 nm this bias was significantly negative (less frequent than expected). At distances >
381 700 nm we again found a positive, but smaller, bias (Fig. 5D).

382 When examining patterns of KEULE foci, we also observed that sites of previous exocytosis
383 events were 3.4 times more likely to show consecutive exocytosis events within 60 seconds than random
384 sites at the plasma membrane (Fig. S5A-E,G). Such "hot spots" were also significantly over-represented
385 within 180 nm of microtubules, but only modestly so (1.25 times more likely) (Fig. S5F,G).

386 Taken together, our results reveal that microtubules spatially organize exocytosis machinery by
387 increasing the frequency of KEULE cluster formation within about 180 nm of the center of the
388 microtubules, a distance about 7 times the dimension of a single microtubule, while at the same time
389 decreasing the probability of KEULE cluster formation distally over a region that is about 3 times as
390 wide. This acts effectively as a concentrating mechanism for KEULE cluster events that is patterned by
391 cortical microtubule organization. As these KEULE clusters overlap heavily in their dynamic
392 characteristics with those observed associated with validated exocytosis events of CSCs, this is strong
393 evidence that microtubule organization of exocytosis is not confined to guiding insertion of CSCs but is a
394 more generalized feature of exocytosis in growing plant cells.

395 **Discussion**

396 To assess imaging of SM/KEULE clusters as a general marker for exocytosis it was important to
397 answer two questions; if there are different types of signal foci that may represent multiple types of
398 cellular structures or functional events, and what features of signal dynamics are associated with
399 exocytotic events. For example, some exocytotic proteins, including V-SNARES and constituents of the
400 exocyst, have been shown to arrive at the site of exocytosis on exocytotic vesicles themselves, while
401 others reside in the cytosol or associate with the plasma membrane and are recruited to the exocytosis site.
402 While we found some evidence for KEULE signal on cytosolic organelles, these foci were relatively rare

403 and were easily identified by their positional dynamics. Further, in experiments using labeled CSCs as a
404 trackable exocytotic cargo, no KEULE signal was detected arriving at validated exocytosis sites on CSC-
405 containing vesicles, indicating that KEULE clusters at the plasma membrane form by recruitment of
406 KEULE to sites of exocytosis after arrival and interaction of cargo-carrying organelles with the plasma
407 membrane. Assembly dynamics of KEULE clusters associated with CSC delivery had similar
408 characteristics as the KEULE cluster population in general, including a wide range of cluster lifetimes
409 ranging from a couple of seconds to half a minute and stereotyped dynamics of signal accumulation and
410 loss. The demonstrated functions of SM proteins in mediating SNARE complex formation and membrane
411 fusion, together with their stereotyped dynamics and tight association with CSC delivery, indicate that
412 dynamic KEULE clusters are valuable markers of individual exocytotic events.

413 Our measurements of thousands of KEULE clusters at the plasma allowed us to analyze patterns
414 of signal accumulation and loss as a function of varying cluster duration - revealing features of, and
415 raising new questions about, the underlying mechanisms of exocytotic machinery assembly, maturation
416 and resolution. Over all durations, KEULE recruitment features an initial phase of rapid accumulation,
417 followed by continued recruitment at a slower rate. This pattern suggests two phases of recruitment with
418 different kinetics. The second rising phase is near linear, indicating a near constant rate of addition over
419 time, characteristic of mechanisms such as polymerization, rather than recruitment of SM proteins to a
420 fixed number of pre-existing binding sites. Such a kinetic might be consistent with the sequential addition
421 of SM-bound SNARE-PINs to a growing chain of laterally-interacting SNARE-PINs at the vesicle-
422 plasma membrane interface[53–55]. This accumulation phase ends and transitions to a plateau, after which
423 signal abruptly decays to non-detectible levels. Both the final signal level and the length of the pause state
424 correlate positively with cluster assembly time, with longer assembly times having higher signal levels
425 and longer pause durations. Over the population of observed events, global peak signal is reached at
426 durations of about 6 seconds, after which longer events involve no further signal accumulation but feature
427 only lengthened plateau times. The plateau phase could represent a state where all the SNARE complexes
428 required have been recruited to the fusion site and the components of the fusion super complex are
429 transitioning to a functionally competent state prior to the enactment of membrane fusion. The plateau
430 could also reflect an assembly checkpoint. Previous *in vitro* studies have found that greater numbers of
431 SNARE proteins are recruited to interfaces of large vesicles and planar membranes[48,49]. It is possible,
432 therefore, that our measurements of KEULE dynamics are shaped in part by a distribution of vesicle sizes,
433 with longer assembly phases that build a brighter SM signal representing assembly of exocytotic
434 machinery at larger vesicles.

435 We found that KEULE dynamics were changed when we disrupted exocytosis with osmotic
436 stress by treatment with mannitol, or by application of a drug, isoxaben. The changes in dynamics were
437 qualitatively different for the two antagonists, indicating that they likely act on different processes
438 affecting exocytosis. These observations indicate that KEULE dynamics, which indicate functional
439 aspects of vesicle fusion, are a sensitive and useful readout, or marker, for studying exocytosis and agents
440 that disrupt or alter exocytosis.

441 High resolution mapping and Bayesian statistical analysis of individual exocytosis events marked
442 by KEULE clusters revealed that these events are not randomly distributed in growing hypocotyl cells but
443 are significantly over-represented in domains defined by the cortical microtubule array. This patterning of
444 exocytosis differs from previously described mechanisms for exocytosis targeting by microtubules. In the
445 latter, the positioning of microtubule plus ends define the locations for motor-transported delivery of
446 either the exocytotic vesicles themselves or proteins that act in defining exocytotic domains. By contrast,
447 our data indicate that the whole microtubule is associated with exocytosis targeting, making the entire
448 cortical array an ordered, dynamic and steerable template for exocytotic patterning and organization of
449 the cell cortex (Fig, 6A). As discussed further below, such highly organized patterning of exocytotic
450 traffic may be useful for creating functional and mechanical asymmetries to support crucial functions like
451 morphogenesis.

452 Our high precision measurements of both microtubule and KEULE cluster locations revealed that
453 microtubules pattern exocytosis both positively and negatively and do so over spatial domains much
454 larger than the scale of microtubules and microtubule bundles. Single microtubules and bundles of two
455 polymers are ~25 nm and ~75 nm wide at the plant cell cortex, respectively[56], whereas the combined
456 width of over-represented and under-represented domains was measured to be ~700 nm. The mean
457 spacing between ordered microtubules and microtubules bundles in elongating hypocotyl cells is about
458 twice this distance[57], indicating that microtubules influence exocytosis over most of the observed plasma
459 membrane these cells (Fig. 6B). In addition, the combination of narrower elevated domains coupled with
460 wider depleted domains of elevated exocytosis frequency suggests a concentrating effect that further
461 enhances the relative difference in exocytosis adjacent to microtubules as compared to distances several
462 hundred nanometers away.

463 One mechanism that could explain the spatial scales of these microtubule-associated domains is
464 direct interaction of exocytotic vesicles with cortical microtubules, such as we previously observed for
465 vesicles containing CSC's[7,58]. Microtubule-tethered vesicles might capture local KEULE associated with
466 the plasma membrane, perhaps as bound to SNARE partners such as SYP121[34], depleting KEULE
467 concentration in the nearby plasma membrane and making exocytosis there less likely, thus creating the
468 observed zones of reduced exocytosis (Fig. 6B). Alternatively, upstream exocytotic machinery, such as
469 plasma-membrane associated components of the exocyst complex, might be recruited by a microtubule-
470 organized membrane domain, elevating location concentration while causing depletion and thus vesicle
471 capture at a distance (Fig. 6B). Evidence that such microtubule-organized membrane domains might exist
472 has been suggested by observations of the plasma membrane associated actin polymerase Formin1, which
473 reveals narrow "dark" linear domains defined by cortical microtubules where fluorescently-tagged
474 Formin1 is excluded[59].

475 The observed flux of KEULE clusters per unit area and time was about 90-fold higher than that
476 measured for CSC delivery, therefore far more exocytosis events are associated with domains defined by
477 microtubules than can be accounted for by CSC delivery alone, implying either that many or most
478 exocytosis events in these cells are influenced by microtubules to some degree, or that a quantitatively
479 significant subpopulation of specialized traffic is redistributed, ~13% of KEULE associated events as
480 measured by our analysis. One possibility for specialized exocytotic traffic targeted by cortical
481 microtubules are cargoes involved in cell wall biosynthesis and cell wall expansion. Supporting this idea
482 is that KEULE has been shown to be an essential partner of the Qa-SNARE SYP121, which is implicated
483 by a growing body of evidence in mediating exocytosis required for cell growth and expansion[19,34,35,60,61].
484 Cellulose is synthesized at the plasma membrane, while many other structural oligosaccharides, such as
485 pectins[62], and wall-active proteins, such as expansins[63], are secreted. Targeting this exocytotic traffic by
486 cortical microtubule arrays to the same locations where newly synthesized cellulose microfibrils are also
487 being laid down could help coordinate the assembly of these diverse components to build a functional cell
488 wall. In addition to coordination of wall assembly, it is possible that the patterned delivery of cell wall
489 oligosaccharides and cell wall active proteins could itself act to support the anisotropic expansion of cell
490 walls required to create specific cell shape. Targeting the delivery of proteins and other molecules that
491 promote wall remodeling by ordered microtubule arrays could create linear and parallel microdomains of
492 increased wall extendibility that lie perpendicular to the main axis of the cell growth - shaping the
493 anisotropy of cell wall expansion in the same direction as proposed in prevailing models for constraint of
494 expansion by cellulose microfibrils organized by microtubules[64]. As discussed in the introduction of this
495 manuscript, an important reason to consider alternative functions for cortical microtubules arrays in
496 guiding cell wall expansion and cell shape is that experimental evidence suggests that guidance of
497 cellulose deposition and CSC delivery alone is not sufficient to explain the anisotropy of cell wall
498 expansion and cell growth. Microtubule targeting of cell wall-active factors by exocytosis could also help
499 explain redirection of cell growth in response to signals, such as blue-light stimulation of phototrophic
500 growth. Perception of blue light by Phototropin receptors causes a rapid 90° reorientation of cortical
501 microtubule arrays[65], but the following redirection of expansion cannot be easily explained by directed

502 cellulose deposition model since previously synthesized cellulose is deposited perpendicular to the
503 direction of expansion. Microtubule patterning of cell wall-active factors might allow for redirection of
504 cell expansion regardless of cellulose orientation.

505 The insights we gained into patterning of exocytosis by cortical microtubule arrays were enabled
506 by utilizing an experimental platform and methods that made detecting, measuring and assessing many
507 thousands of discreet molecular events possible. A protein implicated in mediating a broad swath of a
508 cell's exocytotic traffic might be expected to be subject to a range of targeting mechanisms, including no
509 targeting at all. Such a background could easily obscure a meaningful association between the protein and
510 a hypothesized targeting machinery. Very large sample sizes and appropriate methods to test for
511 meaningful associations, such as we employed here, can robustly reveal such relationships.

512 The fact that growing plant cells have a planar microtubule array that is associated with the
513 plasma membrane, and that exocytotic events as marked by KEULE protein are of relatively low density,
514 has provided an excellent platform to study how microtubules pattern exocytosis, and do so at the level of
515 individual exocytotic events. When we consider cellular microtubule function in cellular trafficking, we
516 typically think of directed transport of cargos by kinesins and dynein. In contrast, this work highlights
517 that microtubules can also function as scaffolds for organizing exocytosis. This scaffolding function for
518 microtubules might be considered in other systems where there is indirect evidence that microtubules
519 regulate exocytosis where they interact with the plasma membrane, such as in focal adhesions and
520 neuronal growth cones[1,66,67]. In addition, scaffolded guidance of exocytosis should also be considered in
521 the context of disease. For example, amyotrophic lateral sclerosis (ALS) risk is associated with genetic
522 variants which reduce levels of functional UNC13A[68,69], and with genetic variation within several
523 microtubule associated proteins[68–71]. It is possible that these proteins all converge on the same biological
524 process of microtubule dependent patterning of exocytosis.

525

526 **Materials and Methods**

527 Generation of transgenic lines

528 The *pKEULE-tdTomato-KEULE* construct was generated by modifying the Gateway-compatible
529 vector pMDC43[72]. A 2049-bp region immediately upstream of the start codon of *KEULE* (At1g12360)
530 was amplified with primers CGTTTAAACTACAGTTCCATTGGAGCAAC and
531 TAGGTACCTGCGATCTAACAATTT CAGACTTC. The tdTomato gene was amplified from a donor
532 vector[73] with primers CAGGTACCATGGTGAGCAAGGGCGAGGAGGT and TGGCGCGCCCTT
533 GTACAGCTCCTCCATGCCGT. The 35S promoter of pMDC43 was exchanged with the *KEULE*
534 upstream regulatory region via PmeI and Acc65I sites, and GFP in pMDC43 was exchanged with
535 *tdTomato* via KpnI and AscI sites. The full-length *KEULE* gene was amplified from genomic DNA using
536 primers GGGGACAAGTTTGTACAAAAAAGCAG GCTTGACCATGTCGTACTCTGACTCC and
537 GGGGACCACTTTGTACAAGAAAGCTGGG TTTATTTGGAGATCGTCTA and then inserted into
538 the modified pMDC43 vector using Gateway cloning technology (Invitrogen) as described previously[65].
539 The construct was introduced into plants heterozygous for the *keule* MM125 deletion allele[37] via
540 Agrobacterium-mediated transformation[74,75]. T2 plants were genotyped for the *KEULE* locus using PCR:
541 primers CGACCTTATCAGAGAGCAAGG and Keu-as0 (ACAGGGATTTGATTTGAGATCTGG)
542 amplified a 1661-bp fragment from the wild-type allele and a 1505-bp allele from the deletion allele.
543 Additionally, the primer pair GTCTGTTAACGGCTGCAGAA and Keu-as0 was used to amplify a
544 fragment (1103 bp) only present in the wild-type allele. A T2 plant homozygous for the deletion allele
545 and hemizygous for the *pKEULE-tdTomato-KEULE* transgene was isolated. A doubly homozygous line
546 was subsequently isolated in the T3 generation and used for experiments.

547 To generate double-labeled plants expressing markers for KEULE protein and cellulose synthase,
548 homozygous *pKEULE-tdTomato-KEULE/ keule* MM125 plants (ecotype Landsberg) were crossed with
549 homozygous *pCESA6-Citrine-CESA6/cesa6prc1-1* plants (ecotype Columbia[14]. An F2 line was selected

550 that was homozygous for both mutations and hemizygous for both markers. In the F3 generation, a
551 quadruply homozygous plant was isolated together with a plant homozygous for both mutations,
552 homozygous for *pCESA6-Citrine-CESA6* and hemizygous for *pKEULE-tdTomato-KEULE*. Seed from the
553 latter plant thus show segregation for the *keule* mutant phenotype.
554 To generate double-labeled plants expressing markers for KEULE protein and microtubules, *p35S-*
555 *EGFP-TUA5* was introduced into *pKEULE-tdTomato-KEULE/keule*-MM125 plants via Agrobacterium-
556 mediated transformation. T2 seedlings expressing the microtubule label were used for experiments.
557
558 Growth
559 Seedlings were grown in the dark on vertical agar plates as described in Lindeboom et al.[65]. For
560 hypocotyl elongation assays, seedlings were grown for 5 days. For live cell imaging experiments,
561 seedlings were imaged 3 days after germination.
562
563 Drug treatments
564 Oryzalin, taxol and isoxaben were dissolved in DMSO for 100x stock solutions. Oryzalin was
565 used at a final concentration of 20 µM, taxol (Sigma) at 20 µM and isoxaben (Sigma) at 100 nM in plant
566 growth media (Hoagland's No. 2). Mannitol was dissolved in plant growth media directly at a
567 concentration of 200 mM. For control treatment (mock), DMSO was added to the growth media to a final
568 concentration of 0.01%. Incubation of the seedlings was performed in 6-well plates (WVR, nontreated)
569 with 2 mL of plant growth media in each well. The plates were wrapped in aluminum foil to block light
570 and incubated at 22 °C. The drug treatment durations were 16 hours for oryzalin, and 2 hours for all other
571 treatments. Likewise, the mock treatments were 16 hours for comparison to oryzalin, and 2 hours for
572 comparison to the remaining treatments.
573
574 Confocal microscopy
575 Imaging was performed on an instrument featuring a CSU-X1 spinning disk head (Yokogawa
576 Electric), a DMI6000 B inverted microscope (Leica), a 100X/1.4 NA oil immersion objective (Leica), an
577 Evolve 512 EMCCD camera (Photometrics) and a 1.2X telescope between the spinning disk unit and
578 camera. EGFP/CITRINE and tdTomato were excited at 488 nm and 561 nm respectively, by solid-state
579 lasers (Coherent Cube). Switching, shuttering and intensity of these lasers was performed by direct
580 electronic control. Emission filtering was accomplished with bandpass filters, (525/50 nm for EGFP and
581 CITRINE and 636/37 nm for tdTomato (SemRock), together with a 405/488/568 nm dichroic filter
582 (SemRock). Exposure times were 400 ms for tdTomato-KEULE, 200 ms for EGFP-TUA5 and 800 ms for
583 Citrine-CESA6. Images were acquired at 1 second intervals in experiments in which both tdTomato-
584 KEULE and EGFP-TUA5 were imaged and 2 second intervals in experiments featuring tdTomato-
585 KEULE together with Citrine-CESA6. All light energies were approximately 4 mW as measured at the
586 end of the optical fiber entering the confocal head. For high-speed acquisitions of tdTomato-KEULE,
587 image streaming was performed at an acquisition rate of 5 Hz (200 ms exposures). The focal plane in all
588 experiments was stabilized by hardware Adaptive Focus Control (Leica) to mitigate changes in specimen
589 intensity over time caused by thermal and mechanical drift in focus.
590 Photobleaching was performed by a Vector laser scanning unit (Intelligent Imaging Innovations)
591 integrated into the setup above at the right camera port. Focused laser light was pulsed and scanned (pulse
592 duration = 10 ms, raster block size = 20 units) on the image plane by a pair of galvanometer-driven
593 mirrors inside the Vector unit. Scanner positions were calibrated to image coordinates using an automated
594 procedure in Slidebook software (Intelligent Imaging Innovations). Citrine photobleaching was performed
595 using the 488 nm laser at the same power as used for imaging but focused on the image plane. Areas of
596 ~200 μm^2 were bleached in 20-30 s.
597 All imaging was performed on the upper hypocotyl cells (1-2 mm below the apical hook).
598 Specimen mounting was performed as described previously[65].
599
600 Image registration

To correct for lateral specimen drift in the movies, we performed image registration in MATLAB. We first performed a running average on the image sequence using a three-frame window (yielding an image series 2 frames shorter than the original series). We then performed an intensity-based image registration algorithm using the MATLAB function imregtform, using tformtype "translation" and conserving the pixel size. To minimize interpolation artifacts, we first determined the transformation matrix that yielded the best intensity match for each consecutive image pair, then calculated the cumulative transformation matrix for the whole averaged image series and applied it to the original movie that was not frame averaged, minus the first and last frame that were lost because of the frame averaging. Some of the KEULE- tdTomato and Citrine-CESA colocalization movies (3 out of 8) still exhibited sample drift after intensity-based registration. In those cases, we applied a feature-based method employing the locations of detected KEULE spots (See Methods: Particle Tracking for details) as registration features and using the MATLAB function estgeotform2d and a rigid transform.

KEULE particle tracking, streaming experiments, image series with labeled microtubules

Particle detection and tracking was performed on the registered movies. For streaming experiments and experiments featuring labeled microtubules (1 second time intervals) we used µTrack[46] to detect and estimate the positions of tdTomato-KEULE clusters in each frame and subsequently link detected foci from frame to frame to track individual KEULE clusters over time. For each experiment type, we used the following parameters:

Streaming image series.

For detection: initial psfSigma = 1.2 pixels, alpha for local max 0.05 and 10 max iterations for psfSigma estimation.

For tracking: max detection gap = 2 frames, min track length = 4 frames, max search radius = 2 pixels, gap penalty = 4.

1-second interval image series.

For detection: initial psfSigma = 1.2 pixels, alpha for local max 0.05 and 10 max iterations for psfSigma estimation.

For tracking: max detection gap = 1 frame, min track length = 1 frames, max search radius = 3 pixels, gap penalty = 4.

KEULE and CESA particle tracking in dual labeled movies

In experiments assessing KEULE localization and dynamics with respect to cellulose synthase complex (CSC) trafficking and we used the Spots module in Imaris software (Bitplane) to detect and track both tdTomato-KEULE clusters and Citrine-CESA6 particles. The Imaris Spots detector and filters performed better for Citrine-CESA6 signals, in particular. CSCs as labeled by Citrine-CESA6 were detected using a size value of 0.3 µm and quality value of 110. Tracking was performed by applying the Autoregressive Motion algorithm (maximum distance = 0.35 µm, maximum gap size = 2 frames). Successful deliveries of CSC complexes to the plasma membrane were determined by dynamic criteria as described previously[7]. Briefly, a delivery event was defined when puncta that were mobile in the streaming cytosol (1) stabilized positionally in the optical plane of the plasma membrane, and (2) showed a transition to slow, steady and linear movement in the velocity range (~200-450 nm/min) we previously have determined be characteristic of CSC's actively synthesizing and extruding cellulose fibers into the cell wall[14]. To make this assessment, we first filtered CSC tracks by duration (>30 seconds), then used a custom GUI in MATLAB to manually inspect and verify each Spots track and associated image data for these characteristics. As a part of this process, the frame in which a tracked particle first showed evidence of stabilized lateral position was marked as the "tethering" frame – the frame showing the time and location of first stable interaction with the cell cortex of a presumed vesicle carrying one or more labeled CSC's.

Clusters of tdTomato-KEULE were detected with Spots module using a size parameter value of 0.3 µm, a quality value of 100 and were tracked using the Connected Components algorithm (frame to frame displacements of KEULE signal are small and not auto-correlated). These settings adequately detected and tracked KEULE clusters based on visual inspection of the results.

Maximum Likelihood Gaussian fitting for particles

We employed maximum likelihood Gaussian fitting as described in Mortensen et al.[47] to use photon counts in estimating the accuracy of particle position and shape. To determine the number of photons collected in each image pixel, we first needed to calibrate our camera gain (photoelectrons per grey value or ADU). Photon detection can be modeled as a Poisson process, which creates a distribution in which the mean equals the variance. Therefore, the camera gain is equal to the coefficient between the mean and variance of the gray values in the image. To calculate this coefficient, we first measured the noise floor of the camera by taking the average of the gray values (intensity) of images acquired with the camera capped. We then determined the grey value variance by subtracting one image from the other then calculating the variance among these pixel-by-pixel difference values. To obtain the final variance, we divided this number by 2 to account for the fact we are using two images for determining the differences. Finally, we calculated the mean intensity of the images, subtracted the noise floor, and divided by the variance to estimate the camera gain.

For each time point in every track, we cropped out a pixel grid with the estimated center of the detected KEULE spot in the middle pixel (9 x 9 pixels). Along with a cropped image, the fitting routine requires a set of initial parameters: xCoordinate, yCoordinate, point spread function standard deviation (PSF SD), background, and an estimate of number of photons that comprise the imaged PSF. The x- and y-coordinates we used are the estimates of position from the particle tracking described above. Based on the approximate emission wavelength and objective numerical aperture, we used 133 nm for the initial standard deviation of the PSF. We estimated the background by calculating the median intensity of the outer border of the pixel grid used for fitting after subtraction of the camera noise floor. If the center of the point source is in the middle of the pixel and the PSF SD is 133 nm, we expect 0.16 of the photoelectrons to be in the center pixel. Therefore, we estimated the number of photoelectrons in the imaged spot by first subtracting the noise floor and pixel background from the intensity in the center pixel and multiplying the result by 1/0.16 (6.25). Before performing fitting using these initial data, we needed to address noise that could have been introduced by bilinear interpolation during the image registration that was employed to mitigate specimen drift. To accomplish this, we used the transformation matrix from registration to map the locations of the tracked particles back to the locations in the original image sequence, we then performed MLE fitting on the non-interpolated images by employing the method of Mortenson et al.[47] in MATLAB.

Since we used free fit parameters and there is noise in the data from photon counting, free fluorescently tagged proteins, high local particle densities and unresolved distributions of labeled structures, we excluded distance measurement from fits that were outside the expected parameter ranges. In the case of the SD of the 2D Gaussian, we found that there was a distinct population where the SD fit parameter was < 50 nm. Since our pixels correspond to 133 nm, in these fits all the photoelectrons are contained in one pixel, which is not consistent for a diffraction-limited spot at the magnification onto our camera (roughly 4 pixels). Similarly, we found that fit SD values above 2x the estimated PSF SD in most cases represented a fit containing more than one particle. Therefore, SD fit results with SD values outside 50 to 266 nm were excluded from position measurements. Fit results with estimated numbers of photoelectrons > 1000 were also considered outliers and excluded. Finally, high local particle densities the distance in some cases caused the MLEwG fit to center on a nearby particle and not the particle marked by the starting position. We therefore also did not include position information for fits where the distance between the original estimate and the MLEwG position differed more than 2 x 133 nm. See Fig. S6 for fit parameters for the tdTomato-KEULE clusters and CIT-CESA6 labeled CSCs.

KEULE to microtubule distance measurements

To determine the position of each KEULE spot to assess the spatial relationship of KEULE accumulation with the microtubule cytoskeleton we first determined the single frame with the highest number of measured photoelectrons for each KEULE track. For tracks that were longer than 4 frames we determined the max number of photoelectrons using a running three frames average, for shorter tracks we did not use frame averaging. The rational for this selection was two-fold. First, we reasoned that maximum signal might best be associated with the site of KEULE function, with initial signal rise being indicative of KEULE recruitment and/or assembly into a membrane fusion structure, and signal loss indicating KEULE disassociation or disassembly of the fusion machinery. Second, the precision of estimated position is proportional to photon sampling. It is also relevant to note that frame-to-frame movement of KEULE tracks were small (Fig. S7).

To locate positions of microtubule signal relative to each KEULE track location, we used a rotating linear filter combined with analysis of signal peaks and a two-step fitting procedure. At the coordinates of KEULE signal in each max value frame we drew a line 21 pixels long and 1 pixel wide extending 10.5 pixels to each side of the KEULE position and repeated this process in increments of 9 degrees to cover 360 degrees (Fig. 4C). We then projected this array of lines on the microtubule channel and extracted the intensities (in photons) along each line at 1-pixel (133 nm) intervals by bilinear interpolation. To locate potential positions of microtubule signal along each sampling angle we used the MATLAB function Findpeaks with a MinPeakProminence of 25 to identify signal peaks. The 10.5-pixel distance is typically long enough to contain the peak intensity of the nearest microtubule. In fact, in many cases this length intersects multiple microtubules, but it is also possible for the end of the lines to partially intersect a microtubule with a peak outside the 10.5 pixels. For subsequent fitting steps, we included pixels from the center until the furthest peak on each side plus 3 pixels to catch the shoulder of these peaks, and at the same time, exclude signal from microtubules whose peaks are just outside the 10.5 pixel range from influencing the fitting. We then estimated the center position of each signal peak by modifying the 2D MLEwG[47] to a quasi-1D version, modeling the microtubule as a Gaussian wall[76] that is one pixel wide, as shown in formula 1 below.

(Formula 1)

$$\mathrm{E} = \mathrm{N}\left(\frac{1}{\sqrt{2\pi\sigma^2}}\right)\left(\frac{1}{w}\right)\exp\left(-\frac{(x-\mu_x)^2}{2\sigma^2}\right) + b^2$$

Where:
E = expected number of photoelectrons per pixel
N = total number of photoelectrons
σ = Standard deviation
w = line width in nm
x = position on the line
μ_x = center position
b^2 = background photoelectrons per pixel

We found up to four peaks on a single line and fitted all peaks simultaneously by adding an additional term describing each additional peak. Formula 2 describes the case for fitting the case for two peaks:

(Formula 2)

$$E = N_{\text{first}}\left(\frac{1}{\sqrt{2\pi\sigma_{\text{first}}^2}}\right)\left(\frac{1}{w}\right)\exp\left(-\frac{(x-\mu_{x\,\text{first}})^2}{2\sigma_{\text{first}}^2}\right) +$$

$$N_{\text{second}}\left(\frac{1}{\sqrt{2\pi\sigma_{\text{second}}^2}}\right)\left(\frac{1}{w}\right)\exp\left(-\frac{(x-\mu_{x\,\text{second}})^2}{2\sigma_{\text{second}}^2}\right)+b_{\text{global}}^2$$

For estimating the seeding parameters for the fit, we used the center of the maximum value pixel for each peak identified by Findpeaks. We used 160 nm (median value of the peak population) as the estimate for the standard deviation and we approximated the background by taking the square root of the lowest 10 percentile of all the pixels for all angles after subtracting the noise floor.

After fitting all microtubule peaks along all angular steps, we determined the distance from the KEULE location to the center of the nearest microtubule signal. We did this in three steps. First, we determined the nearest microtubule signal peak to the KEULE location from among the initial angular samples. Second, we determined the angle of the microtubule identified by the closest peak. Measuring the distance from the KEULE location to the center of the microtubule signal is most accurate along a line perpendicular from the KEULE location to the microtubule. By determining the local microtubule signal angle, we could then determine the optimal perpendicular sample angle. To find the local orientation of the microtubule we rotated a line of 21 pixels long around the center of the location where we initially found the closest microtubule peak. We extracted the summed signal intensities along these lines and determined the angle at which we found the maximum intensity, corresponding to the microtubule angle[69]. Finally, once we established the microtubule angle, we used the angle perpendicular to that microtubule angle to extract the nearest microtubule fit for the representative KEULE position. Distance values where the fit parameters for the microtubule positions were the number of photoelectrons were < 50 or > 10000, as well as SD fit parameters < 50 or > 250 nm were excluded from distance measurements. We required all the microtubule fits on the line to be within these parameters to be included in the analysis. See Fig. S8A-C for fit parameters for KEULE (A) and microtubule signal (B) fits after selection as well as the standard error of the distance measurement between them (C).

Analysis of KEULE localization with CESA6 delivery sites

KEULE and CESA6 spots were detected and tracked in Imaris as described above and maximum likelihood 2D Gaussian fitting was applied to each set of tracks. CESA tracks tend to be relatively long and can be confounded by a dynamic background produced by highly motile CESA containing organelles including Golgi bodies and Trans-Golgi network compartments. This background makes fully automated detection and quantitation of CSC delivery events challenging. We therefore designed a graphical user interface in MATLAB that allowed us to efficiently curate potential CESA delivery events identified in Imaris and verify whether individual tracks were indeed depicting a CESA delivery. We have shown previously that CESA delivery to the plasma membrane typically shows three distinct phases; (1) erratic movement of CESA containing vesicles as they appear in the optical plane at the cell cortex, (2) positional-stabilization and (3) slow and steady movement with typically linear trajectories. We speculate that the second phase represents molecular tethering at the plasma membrane and the events that lead to vesicle fusion and cargo delivery. The third phase is behavior that we have shown is characteristic of active CSC complexes in the plasma membrane as they synthesize cellulose[14]. Thus, observation of this latter behavior indicates successful delivery of CESA cargo to the plasma membrane. For each CESA track that showed these three distinct phases, we marked the first frame of CESA stabilization at the plasma membrane. From this position, we determined the distance to the nearest KEULE spot in a 30-frame time range (60 seconds). Some degree of coincidence between CESA deliveries and KEULE spots is expected by chance alone, especially since the density of KEULE clusters at the plasma membrane is relatively high. To evaluate whether the observed distribution of KEULE locations with sites of CESA stabilization might be due to chance alone, we generated random positions in the same regions of interest used for the experimental data and calculated the distances to the nearest KEULE spot. We used these simulated data to model the expected distribution of distances and compared this distribution to the

distribution of distances found for confirmed CESA delivery events. First, we divided both the experimental and simulated distance distributions up into 40 nm distance bins and calculated the bin-by-bin count frequencies by the total number of simulated counts. We then introduced a bias parameter δ that equates an observed frequency in each distance bin to the expected value from the simulated distribution as shown in formula (4).

(Formula 4)

$$P_{inDistBin}(\delta) = \frac{\text{Expected}_{inDistBin}\,\delta}{Expected_{\text{inDistBin}}\,\delta + \text{Expected}_{\text{outsideDistBin}}(1-\delta)}$$

The value of δ may vary between 0 and 1. For a possible observed frequency that equals the expected frequency, δ is equal 0.5. If δ is greater than 0.5, an observed frequency is higher than expected. Likewise, if δ is less than 0.5 the observed frequency lower than expected under the null hypothesis. Use of the parameter allows us to use a Bayesian approach to test multiple hypotheses to ask what bias value best may best explain the actual observed frequencies. To do this, we calculated the Likelihood Ratio of observing an experimental result given a range of values for δ (in increments of 0.001, excluding 0) for each frequency bin:

(Formula 5)

$$\frac{L(\delta)}{L\frac{1}{2}} = \frac{P_{inDistBin}\,(\delta)^{M}\,(1\,-\,P_{inDistBin}\,(\delta)^{N-M})}{Expected^{N}_{inDistBin}\,Expected^{N-M}_{outsideDistBin}}$$

Where:
$L(\delta)$ = likelihood of the data given the bias δ,
$L\frac{1}{2}$ = likelihood of the data in the neutral case (no positive or negative bias)
N = total number of measurements
M = number of measurements in this specific distance bin

We then found the maximum a posteriori probability (MAP) for δ and computed the shortest range of δ values for the highest posterior density (HPD) that contains 95% of the normalized probability density. Maximum likelihood estimates for δ below 0.5 indicate underrepresentation at the distance of interest and above 0.5 indicate overrepresentation of experimental data compared to the unbiased case.

Analysis of KEULE localization with microtubules

We used the same Bayesian approach describe above for analyzing the localization of KEULE clusters with respect to the estimated center of the nearest microtubule. We changed the distance bin size from 40 to 20 nm.

Hot spot analysis

To investigate if some KEULE events are independent of each other each or not (e.g. if "hot spots" for KEULE accumulation may exist), we examined colocalization between sequential KEULE spots in time series collected from cells expressing both labeled KEULE and tubulin proteins. Within a region of interest in each time series, we selected all KEULE tracks that were first detected between frames 2 and 31 and calculated the distance to all other KEULE tracks that started subsequently up to and including frame 301. For position estimates we used the frame in the track that showed the highest number of fitted photoelectrons. To compare the degree of colocalization of the initial KEULE tracks with future KEULE tracks to that expected from chance alone, we created a simulated initial dataset with random locations within the same region of interest and calculated the distances to all KEULE tracks in the same time range.

Since KEULE foci are positionally stable (Fig. S7) we chose a stringent distance threshold of 133 nm (1 pixel) to declare two spots or locations to be co-localized. Because of the relatively high density of KEULE spots at the plasma membrane, colocalization is expected at some point in time, therefore the time frame of colocalization analysis is also important. Indeed, we observe a large degree of colocalization in the whole dataset for both the experimental and simulated data, but with very distinct waiting time distributions (Fig. S5D). Based on the differences in the distribution of waiting times between random simulated positions and KEULE positions until the next KEULE spot arrives, we determined that a 40 second time delay window captures most biologically relevant colocalizations while excluding most random colocalizations due to KEULE density and chance.

853 **Bibliography**

854 1. Noordstra, I. & Akhmanova, A. Linking cortical microtubule attachment and exocytosis. *F1000Research* **6**, 469
855 (2017).

856 2. Spiliotis, E. T. & Nelson, W. J. Spatial control of exocytosis. *Curr. Opin. Cell Biol* **15**, 430–437 (2003).

857 3. Fourriere, L., Jimenez, A. J., Perez, F. & Boncompain, G. The role of microtubules in protein transport. *Journal*
858 *of Cell Science* **133**, 237016 (2020).

859 4. Chang, F. & Martin, S. G. Shaping Fission Yeast with Microtubules. *Cold Spring Harb. Perspect. Biol* **1**,
860 001347 (2009).

861 5. Bartolini, F. & Gundersen, G. G. Generation of noncentrosomal microtubule arrays. *J. Cell Sci* **119**, 4155–4163
862 (2006).

863 6. Shaw, S. L., Kamyar, R. & Ehrhardt, D. W. Sustained Microtubule Treadmilling in Arabidopsis Cortical
864 Arrays. *Science* **300**, 1715–1718 (2003).

865 7. Gutierrez, R., Lindeboom, J. J., Paredez, A. R., Emons, A. M. C. & Ehrhardt, D. W. Arabidopsis cortical
866 microtubules position cellulose synthase delivery to the plasma membrane and interact with cellulose synthase
867 trafficking compartments. *Nat. Cell Biol* **11**, 797–806 (2009).

868 8. Sampathkumar, A. *et al.* Patterning and Lifetime of Plasma Membrane-Localized Cellulose Synthase Is
869 Dependent on Actin Organization in Arabidopsis Interphase Cells. *Plant Physiol* **162**, 675–688 (2013).

870 9. Vellosillo, T., Dinneny, J. R., Somerville, C. R. & Ehrhardt, D. W. TRANVIA (TVA) facilitates cellulose
871 synthase trafficking and delivery to the plasma membrane. *Proc. Natl. Acad. Sci* **118**, 2021790118 (2021).

872 10. Li, S., Lei, L., Somerville, C. R. & Gu, Y. Cellulose synthase interactive protein 1 (CSI1) links microtubules
873 and cellulose synthase complexes. *Proc. Natl. Acad. Sci* **109**, 185–190 (2012).

874 11. Bringmann, M. *et al.* POM-POM2/CELLULOSE SYNTHASE INTERACTING1 Is Essential for the
875 Functional Association of Cellulose Synthase and Microtubules in Arabidopsis. *Plant Cell* **24**, 163–177 (2012).

876 12. Zhu, X., Li, S., Pan, S., Xin, X. & Gu, Y. CSI1, PATROL1, and exocyst complex cooperate in delivery of
877 cellulose synthase complexes to the plasma membrane. *Proc. Natl. Acad. Sci* **115**, 3578–3587 (2018).

878 13. Lei, L. *et al.* CELLULOSE SYNTHASE INTERACTIVE1 Is Required for Fast Recycling of Cellulose
879 Synthase Complexes to the Plasma Membrane in Arabidopsis. *The Plant Cell* **27**, 2926–2940 (2015).

880 14. Paredez, A. R., Somerville, C. R. & Ehrhardt, D. W. Visualization of Cellulose Synthase Demonstrates
881 Functional Association with Microtubules. *Science* **312**, 1491–1495 (2006).

882 15. DeBolt, S. *et al.* Morlin, an inhibitor of cortical microtubule dynamics and cellulose synthase movement. *Proc.*
883 *Natl. Acad. Sci* **104**, 5854–5859 (2007).

884 16. Emons, A. M. C., Mulder, B. M., Emons, A. M. C. & Mulder, B. M. How the deposition of cellulose
885 microfibrils builds cell wall architecture. *Trends Plant Sci* **5**, 35–40 (2000).

886 17. Hamant, O. *et al.* Developmental Patterning by Mechanical Signals in Arabidopsis. *Science* **322**, 1650–1655
887 (2008).

888 18. Zhang, B., Karnik, R., Alvim, J., Donald, N. & Blatt, M. R. Dual Sites for SEC11 on the SNARE SYP121
889 Implicate a Binding Exchange during Traffic1. *Plant Physiol* **180**, 228–239 (2019).

890 19. Honsbein, A. *et al.* A tripartite SNARE-K+ channel complex mediates in channel-dependent K+ nutrition in
891 Arabidopsis. *Plant Cell* **21**, 2859–2877 (2009).

892 20. Assaad, F. F. *et al.* The PEN1 Syntaxin Defines a Novel Cellular Compartment upon Fungal Attack and Is
893 Required for the Timely Assembly of Papillae. *Mol. Biol. Cell* **15**, 5118–5129 (2004).

894 21. Bloch, D. *et al.* Exocyst SEC3 and Phosphoinositides Define Sites of Exocytosis in Pollen Tube Initiation and
895 Growth. *Plant Physiol* **172**, 980–1002 (2016).

896 22. Fendrych, M. *et al.* Visualization of the exocyst complex dynamics at the plasma membrane of Arabidopsis
897 thaliana. *MBoC* **24**, 510–520 (2013).

898 23. Barg, S., Knowles, M. K., Chen, X., Midorikawa, M. & Almers, W. Syntaxin clusters assemble reversibly at
899 sites of granules in live cells. in *Proceedings of the National Academy of Sciences* vol. 107 20804–20809
900 (2010).

901 24. Knowles, M. K. *et al.* Single granules of live cells recruit syntaxin-1 and synaptosomal associated protein 25
902 (SNAP-25) in large copy numbers. in *Proceedings of the National Academy of Sciences* vol. 107 20810–20815
903 (2010).

904 25. McNew, J. A. *et al.* Close Is Not Enough. *The Journal of Cell Biology* **150**, 105–118 (2000).

905 26. Südhof, T. C. & Rothman, J. E. Membrane Fusion: Grappling with SNARE and SM Proteins. *Science* **323**,
906 474–477 (2009).

907 27. Burgoyne, R. D. *et al.* The Functions of Munc18-1 in Regulated Exocytosis. *Ann. N. York Acad. Sci* **1152**, 76–
908 86 (2009).

909 28. Baker, R. W. *et al.* A direct role for the Sec1/Munc18-family protein Vps33 as a template for SNARE
910 assembly. *Science* **349**, 1111–1114 (2015).

911 29. Stepien, K. P., Prinslow, E. A. & Rizo, J. Munc18-1 is crucial to overcome the inhibition of synaptic vesicle
912 fusion by αSNAP. *Nat. Commun* **10**, 4326 (2019).

913 30. Peng, R.-W., Guetg, C., Abellan, E. & Fussenegger, M. Munc18b regulates core SNARE complex assembly
914 and constitutive exocytosis by interacting with the N-peptide and the closed-conformation C-terminus of
915 syntaxin 3. *Biochem. J* **431**, 353–361 (2010).

916 31. Hashizume, K., Cheng, Y.-S., Hutton, J. L., Chiu, C. & Carr, C. M. Yeast Sec1p Functions before and after
917 Vesicle Docking. *Mol. Biol. Cell* **20**, 4673–4685 (2009).

918 32. Mayer, U., Ruiz, R. A. T., Berleth, T., Miséra, S. & Jürgens, G. Mutations affecting body organization in the
919 Arabidopsis embryo. *Nature* **353**, 402–407 (1991).

920 33. Assaad, F. F., Mayer, U., Wanner, G. & Jürgens, G. The KEULE gene is involved in cytokinesis in
921 Arabidopsis. *Mol. Gen. Genet. MGG* **253**, 267–277 (1996).

922 34. Karnik, R. *et al.* Arabidopsis Sec1/Munc18 protein SEC11 is a competitive and dynamic modulator of SNARE
923 binding and SYP121-dependent vesicle traffic. *Plant Cell* **25**, 1368–1382 (2013).

924 35. Karnik, R. *et al.* Binding of SEC11 indicates its role in SNARE recycling after vesicle fusion and identifies two
925 pathways for vesicular traffic to the plasma membrane. *Plant Cell* **27**, 675–694 (2015).

926 36. Karnahl, M. *et al.* Functional diversification of Arabidopsis SEC1-related SM proteins in cytokinetic and
927 secretory membrane fusion. *Proceedings of the National Academy of Sciences* **115**, 6309–6314 (2018).

928 37. Assaad, F. F., Huet, Y., Mayer, U. & Jürgens, G. The Cytokinesis Gene KEULE Encodes a Sec1 Protein That
929 Binds the Syntaxin Knolle. *The Journal of Cell Biology* **152**, 531–544 (2001).

930 38. Carr, C. M., Grote, E., Munson, M., Hughson, F. M. & Novick, P. J. Sec1p Binds to SNARE Complexes and
931 Concentrates at Sites of Secretion. *J. Cell Biol* **146**, 333–344 (1999).

932 39. Scott, B. L. *et al.* Sec1p directly stimulates SNARE-mediated membrane fusion in vitro. *J. Cell Biol* **167**, 75–85
933 (2004).

934 40. Zilly, F. E., Sørensen, J. B., Jahn, R. & Lang, T. Munc18-Bound Syntaxin Readily Forms SNARE Complexes
935 with Synaptobrevin in Native Plasma Membranes. *PLoS Biol* **4**, 330 (2006).

936 41. Medine, C. N., Rickman, C., Chamberlain, L. H. & Duncan, R. R. Munc18-1 prevents the formation of ectopic
937 SNARE complexes in living cells. *J. Cell Sci* **120**, 4407–4415 (2007).

938 42. Rickman C. & Duncan R. R. Munc18/Syntaxin Interaction Kinetics Control Vesicle Dynamics2. *J. Biol. Chem*
939 **285**, 3965–3972 (2010).

940 43. Smyth, A. M., Rickman, C. & Duncan, R. R. Vesicle Fusion Probability Is Determined by the Specific
941 Interactions of Munc18*. *J. Biol. Chem* **285**, 38141–38148 (2010).

942 44. Trexler, A. J., Sochacki, K. A. & Taraska, J. W. Imaging the recruitment and loss of proteins and lipids at
943 single sites of calcium-triggered exocytosis. *Mol. Biol. Cell* **27**, 2423–2434 (2016).

944 45. Somasundaram, A. & Taraska, J. W. Local protein dynamics during microvesicle exocytosis in neuroendocrine
945 cells. *Mol. Biol. Cell* **29**, 1891–1903 (2018).

946 46. Jaqaman, K. *et al.* Robust single-particle tracking in live-cell time-lapse sequences. *Nat. Methods* **5**, 695–702
947 (2008).

948 47. Mortensen, K. I., Churchman, L. S., Spudich, J. A. & Flyvbjerg, H. Optimized localization analysis for single-
949 molecule tracking and super-resolution microscopy. *Nat. Methods* **7**, 377–381 (2010).

950 48. Cho, W. J., Jeremic, A. & Jena, B. P. Size of Supramolecular SNARE Complex: Membrane-Directed Self-
951 Assembly. *J. Am. Chem. Soc* **127**, 10156–10157 (2005).

952 49. Cho, W. J. *et al.* Membrane-directed molecular assembly of the neuronal SNARE complex. *J. Cell. Mol. Med*
953 **15**, 31–37 (2011).

954 50. Haigler, C. H. & Brown, R. M. Transport of rosettes from the golgi apparatus to the plasma membrane in
955 isolated mesophyll cells ofZinnia elegans during differentiation to tracheary elements in suspension culture.
956 *Protoplasma* **134**, 111–120 (1986).

957 51. Zhang, Y. *et al.* Golgi-localized STELLO proteins regulate the assembly and trafficking of cellulose synthase
958 complexes in Arabidopsis. *Nat. Commun* **7**, 11656 (2016).

959 52. Scheible, W.-R., Eshed, R., Richmond, T., Delmer, D. & Somerville, C. Modifications of cellulose synthase
960 confer resistance to isoxaben and thiazolidinone herbicides in Arabidopsis Ixr1 mutants. in *Proceedings of the*
961 *National Academy of Sciences* vol. 98 10079–10084 (2001).

962 53. Zhou, Q. *et al.* Architecture of the synaptotagmin–SNARE machinery for neuronal exocytosis. *Nature* **525**, 62–
963 67 (2015).

964 54. Brunger, A. T. Structure and function of SNARE and SNARE-interacting proteins. *Q Rev Biophys* **38**, 1–47
965 (2005).

966 55. Rothman, J. E., Krishnakumar, S. S., Grushin, K. & Pincet, F. Hypothesis – buttressed rings assemble, clamp,
967 and release SNAREpins for synaptic transmission. *FEBS Lett* **591**, 3459–3480 (2017).

968 56. Giddings, T. H. & Staehelin, L. A. Spatial relationship between microtubules and plasma-membrane rosettes
969 during the deposition of primary wall microfibrils in Closterium sp. *Planta* **173**, 22–30 (1988).

970 57. Lindeboom, J. J. *et al.* CLASP stabilization of plus ends created by severing promotes microtubule creation and
971 reorientation. *J. Cell Biol* **218**, 190–205 (2019).

972 58. Crowell, E. F. *et al.* Pausing of Golgi Bodies on Microtubules Regulates Secretion of Cellulose Synthase
973 Complexes in Arabidopsis. *Plant Cell* **21**, 1141–1154 (2009).

974 59. Martinière, A., Gayral, P., Hawes, C. & Runions, J. Building bridges: formin1 of Arabidopsis forms a
975 connection between the cell wall and the actin cytoskeleton. *Plant J* **66**, 354–365 (2011).

976 60. Geelen, D. *et al.* The abscisic acid-related SNARE homolog NtSyr1 contributes to secretion and growth:
977 evidence from competition with its cytosolic domain. *Plant Cell* **14**, 387–406 (2002).

978 61. Grefen, C. *et al.* A novel motif essential for SNARE interaction with the K(+) channel KC1 and channel gating
979 in Arabidopsis. *Plant Cell* **22**, 3076–3092 (2010).

980 62. Hoffmann, N., King, S., Samuels, A. L. & McFarlane, H. E. Subcellular coordination of plant cell wall
981 synthesis. *Dev. Cell* **56**, 933–948 (2021).

982 63. Cosgrove, D. J. Plant expansins: diversity and interactions with plant cell walls. *Curr. Opin. Plant Biol* **25**,
983 162–172 (2015).

64. Baskin, T. I. ANISOTROPIC EXPANSION OF THE PLANT CELL WALL. *Annu. Rev. Cell Dev. Biol* **21**, 203–222 (2005).

65. Lindeboom, J. J. *et al.* A Mechanism for Reorientation of Cortical Microtubule Arrays Driven by Microtubule Severing. *Science* **342**, 1245533 (2013).

66. Baas, P. W., Rao, A. N., Matamoros, A. J. & Leo, L. Stability properties of neuronal microtubules. *Cytoskeleton* **73**, 442–460 (2016).

67. Tojima, T., Itofusa, R. & Kamiguchi, H. Steering Neuronal Growth Cones by Shifting the Imbalance between Exocytosis and Endocytosis. *The Journal of Neuroscience* **34**, 7165–7178 (2014).

68. Brown, A.-L. *et al.* TDP-43 loss and ALS-risk SNPs drive mis-splicing and depletion of UNC13A. *Nature* **603**, 131–137 (2022).

69. Ma, X. R. *et al.* TDP-43 represses cryptic exon inclusion in the FTD–ALS gene UNC13A. *Nature* **603**, 124–130 (2022).

70. Liu, X. & Henty-Ridilla, J. L. Multiple roles for the cytoskeleton in ALS. *Exp. Neurol* **355**, 114143 (2022).

71. Zhang, S. *et al.* Genome-wide identification of the genetic basis of amyotrophic lateral sclerosis. *Neuron* **110**, 992-1008 11 (2022).

72. Curtis, M. D. & Grossniklaus, U. A Gateway Cloning Vector Set for High-Throughput Functional Analysis of Genes in Planta. *Plant Physiol* **133**, 462–469 (2003).

73. Shaner, N. C. *et al.* Improved monomeric red, orange and yellow fluorescent proteins derived from Discosoma sp. red fluorescent protein. *Nat. Biotechnol* **22**, 1567–1572 (2004).

74. Clough, S. J. & Bent, A. F. Floral dip: a simplified method for Agrobacterium -mediated transformation of Arabidopsis thaliana. *Plant J* **16**, 735–743 (1998).

75. Logemann, E., Birkenbihl, R. P., Ülker, B. & Somssich, I. E. An improved method for preparing Agrobacterium cells that simplifies the Arabidopsis transformation protocol. *Plant Methods* **2**, 16 (2006).

76. Ruhnow, F., Zwicker, D. & Diez, S. Tracking Single Particles and Elongated Filaments with Nanometer Precision. *Biophys. J* **100**, 2820–2828 (2011).

Acknowledgments: We thank Michael Davidson for the kind gift of the tdTomato construct. We thank Zdeněk Lánský, Johnathan Cooper-Knock and Masayoshi Nakamura for advice and insightful comments.

Funding: National Institutes of Health grant R15GM137247-01 (VK), National Institutes of Health grant R01GM123259-01 (DWE)

Author contributions:

Conceptualization: JJL, RG, VK, DWE

Methodology: JJL, RG, VK, DWE

Investigation: JJL, RG, VK, DWE

Visualization: JJL, RG, DWE

Funding acquisition: VK, DWE

Writing – original draft: JJL, RG, DWE

Writing – review & editing: JJL, RG, VK, DWE

Competing interests: The authors declare no competing interests.

Data and materials availability: Biological material, raw data, processed data and MATLAB scripts used for the analysis are available upon request.

1027 **Figures**

1028 **Figure 1**

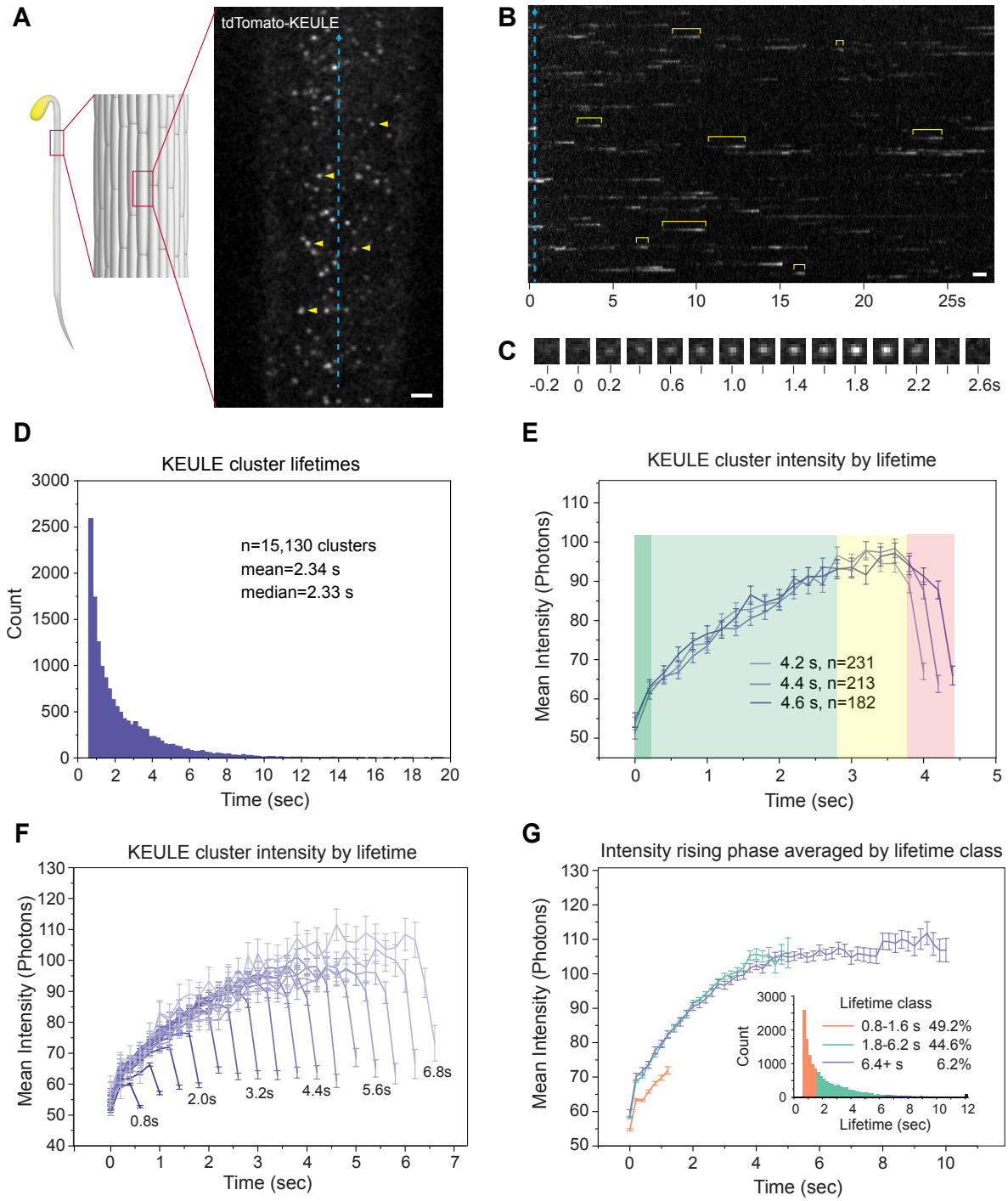

1029

1030 **Fig. 1. KEULE assembly dynamics at the plasma membrane**. (**A**) Distribution of tdTomato-KEULE
1031 signal at the plasma membrane of etiolated hypocotyl cells in *Arabidopsis*. Arrowheads point out
1032 individual clusters of labeled KEULE protein. (**B**) Kymograph of the tdTomato-KEULE signal intensity
1033 over time as sampled over the transect line shown in (**A**) (blue dashes). The yellow brackets highlight
1034 several individual tdTomato-KEULE clusters. (**C**) Example of tdTomato-KEULE cluster intensity over
1035 time. (**D**) Histogram of KEULE cluster lifetimes in 200 ms bins. n = 15,130 clusters. (**E**) Average
1036 tdTomato-KEULE cluster signal intensity with a lifetime of 4.2, 4.4 and 4.6 s. Note the initial rapid
1037 increase in signal over the first acquisition step (darker green), the more gradual, near linear, ramp up
1038 (green) to a plateau (yellow), followed by abrupt loss to non-detection (red). n = 231, 213,182 clusters for
1039 4.2, 4.4 4.8 s, respectively. (**F**) Average tdTomato-KEULE cluster signal intensity with lifetimes ranging
1040 from 0.8 to 6.8 s. n = 15,397 clusters in total, ranging from 4992 clusters for 0.8 s to 122 for 6.8 s. (**G**)
1041 Average signal intensities of tdTomato-KEULE clusters in three cumulative lifetime ranges, 0.8 to 1.6 s,
1042 1.8 to 6.2 s and 6.4+ s. The inset shows the lifetime distribution histogram of tdTomato-KEULE cluster
1043 lifetimes with the lifetime ranges color coded. n = 15,130 clusters. All data in panels D-G acquired from
1044 12 cells from 12 seedlings. Error bars are S.E. Scale bars are 2 µm.

1045 **Figure 2**

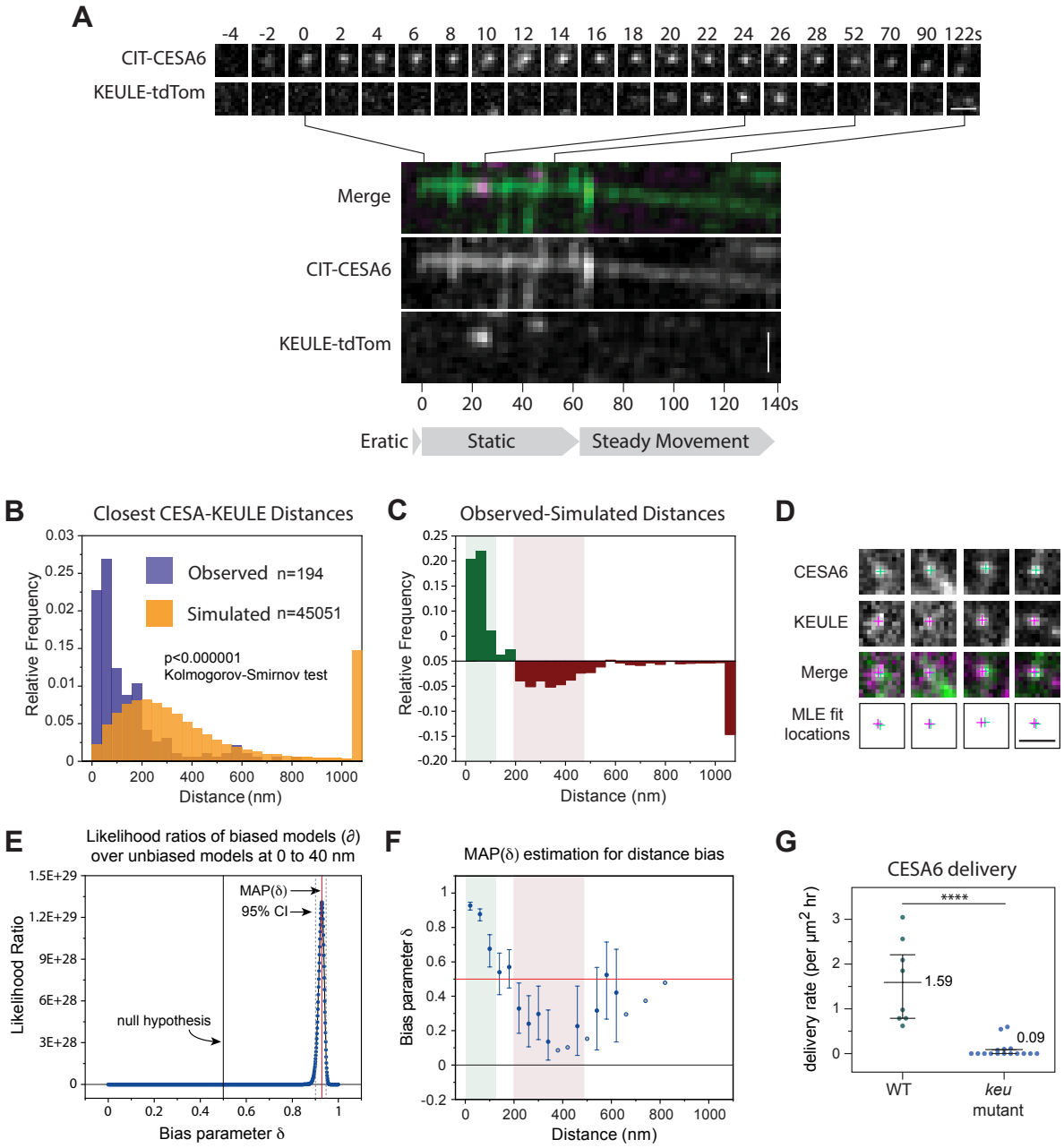

1046
1047

1048 **Fig. 2. KEULE is spatially associated with and required for CSC delivery to the plasma membrane.**
1049 (**A**) CESA exocytosis event. (Top panel) Time series (top panel) and kymograph (bottom panel) of
1050 tdTomato-KEULE and CIT-CESA6 during a CESA exocytosis event. The kymograph shows evidence for
1051 CSC-vesicle tethering at the plasma membrane (start of static phase) and successful CSC delivery to the
1052 plasma membrane as an active complex (steady movement phase, see text). (**B**) Distribution of distances
1053 between the positions of CIT-CESA6 signals at start of static phase and the nearest tdTomato-KEULE
1054 cluster, as estimated by MLE PSF fitting. Data shown both for observed CIT-CESA6 locations and
1055 simulated random locations. (**C**) Differences of the observed vs expected CESA6-KEULE distance
1056 frequencies in (**B**), portraying over- and under-representation (green and red respectively). (**D**) Examples
1057 of colocalization and fitted positions for events in (**B**). (**E**) Bayesian likelihood ratios of the observed
1058 frequency of distances between 0 and 40 nm given bias δ over $\delta(0.5)$. The position of the peak value
1059 indicates the most likely, or maximum a posteriori probability (MAP), value for the bias δ for the
1060 observed frequency given the expected frequency. (**F**) Bayesian analysis of the MAP(δ) for each distance
1061 bin, MAP(δ) = 0.5 indicates no difference from expected. Error bars are 95% confidence intervals
1062 expressed as the highest posterior density (HPD, the shortest interval containing 95% of the probability
1063 density). (**G**) CESA6 delivery rates in wild type and *keule* mutant cells. Whiskers are quartiles. ****
1064 $p<0.0001$ Wilcoxon 2-sample test. In panels B-F, n = 194 CESA exocytosis events in 8 cells from 8
1065 seedlings for observed data. For simulated data, n = 45051 randomized CESA exocytosis locations in the
1066 same KEULE channel data sets. In panel G, n = 8 cells from 8 seedlings for WT and 16 cells from 16
1067 plants for *keule*. Scale bars are 1 μm.

1068 **Figure 3**

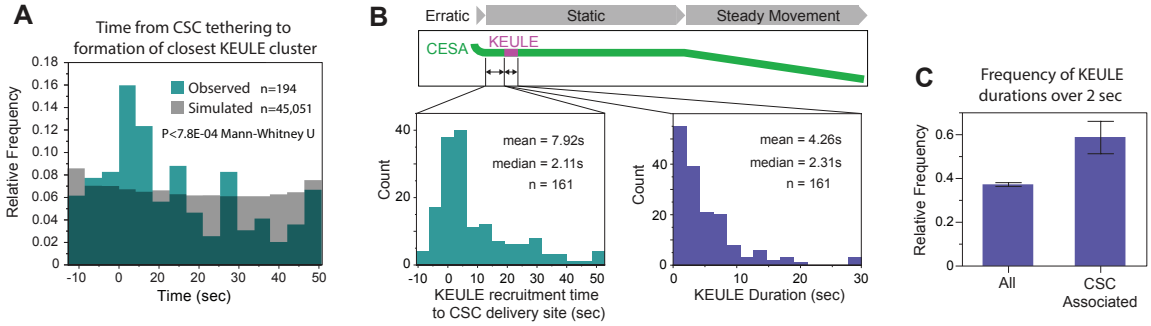

1069

1070 **Fig. 3. KEULE cluster appearance is temporally associated with CSC appearance at the plasma**
1071 **membrane.** (**A**) Comparison of the waiting time distribution from CSC signal stabilization until the
1072 detection of the nearest tdTomato-KEULE cluster in observed and simulated data. n = 194 CSC delivery
1073 events in 8 cells from 8 plants. (**B**) KEULE dynamics in the context of CSC delivery to the plasma
1074 membrane. Histograms of waiting times (left pane) and lifetimes of tdTomato-KEULE clusters co-
1075 localized with CSC delivery events (right pane). n = 161 CSC delivery events in 8 cells from 8 plants for
1076 observed data, n = 45,051 simulated CSC delivery events applied to the same data sets. (**C**) KEULE
1077 cluster durations for all events and those associated with CSC delivery, compared by relative frequency of
1078 durations over 2 seconds. n = 13766 for all KEULE clusters, n = 180 for KEULE clusters associated with
1079 CSC delivery. Whiskers are exact binomial 95% confidence intervals, p = 6.1E-09 Fishers' exact test.

1080 **Figure 4**

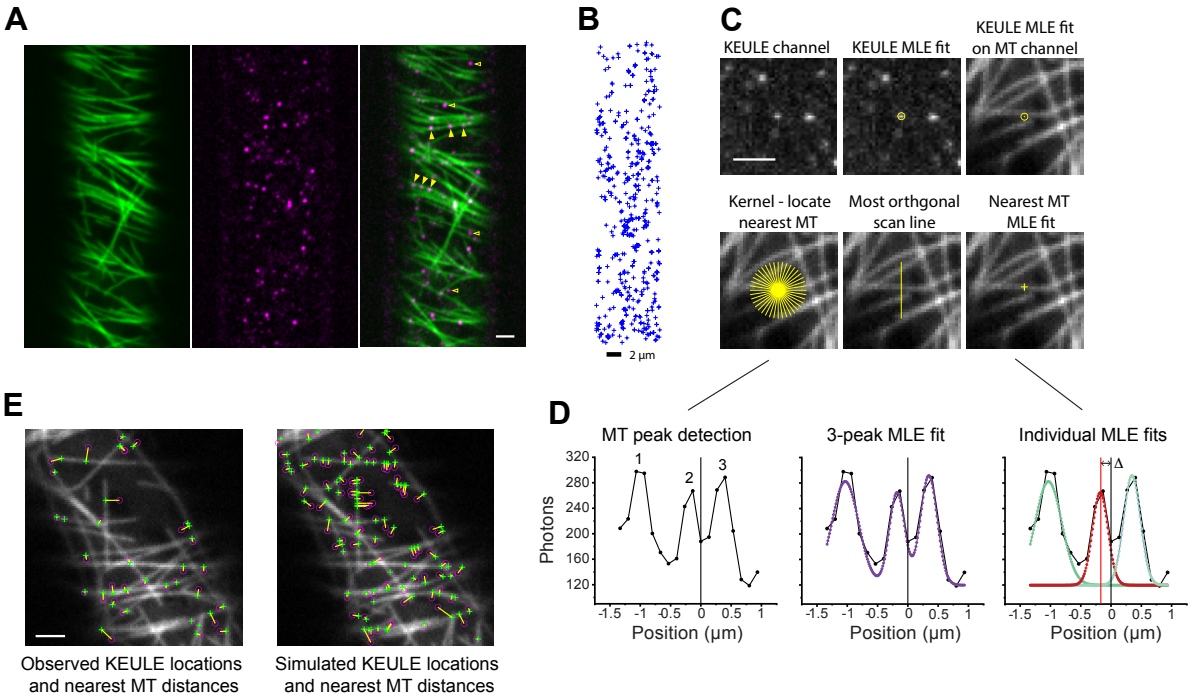

1081
1082 **Fig. 4. Microtubule dependent distribution of exocytosis events.** (**A**) Images of GFP-TUA5 and
1083 tdTomato-KEULE signal in epidermal cells. Arrowheads indicate examples of apparent co-localization of
1084 signal. (**B**) Spatial patterning of tdTomato-KEULE clusters over the range of 36.8 seconds. Crosses show
1085 positions of MLEwG fits. (**C**) Steps in the routine employed to calculation the distance from a KEULE
1086 cluster to the center of the nearest microtubule distance. (**D**) Steps in quasi-1-dimensional MLEwG fitting
1087 of microtubule signal along the most-orthogonal scan line of a rotating filter. (**E**) Overlay of a
1088 microtubule channel image and pairs of markers for MLE fit locations of KEULE clusters and the center
1089 of the nearest microtubule in observed data (left) and for simulated random KEULE locations (right).
1090 KEULE cluster detects from -5 to + 5 frames from the microtubule image are shown. Scale bars are 2 µm.

1091 **Figure 5**

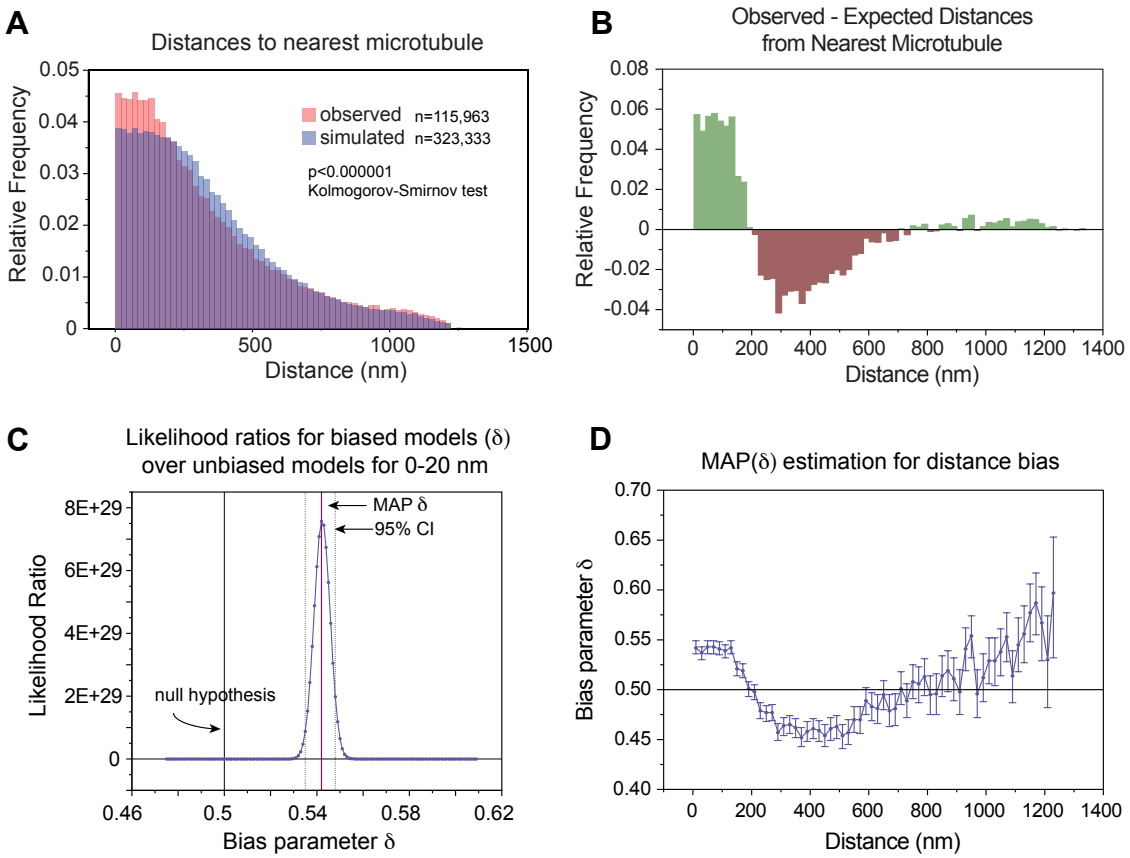

1092

1093 **Fig. 5. Bayesian analysis of microtubule bias for exocytosis events.** (**A**) Comparison of the
1094 distributions of KEULE-nearest microtubule distances for observed and simulated data. n = 115,963
1095 KEULE clusters in 14 cells from 14 plants. (**B**) Differences of the observed vs expected KEULE-
1096 microtubule distance frequencies shown in (**A**), portraying the pattern of over- and under-representation
1097 (green and red respectively). (**C**) Bayesian likelihood ratios of the observed frequency of KEULE-
1098 microtubule distances between 0 and 20 nm given bias δ over δ(0.5). (**D**) Bayesian analysis of the
1099 MAP(δ) of each distance bin. Data acquired from 14 cells in 14 seedlings. n = 115,963 KEULE clusters
1100 in 14 cells from 14 plants. Error bars are 95% confidence intervals expressed as HPD.

1101 **Figure 6**

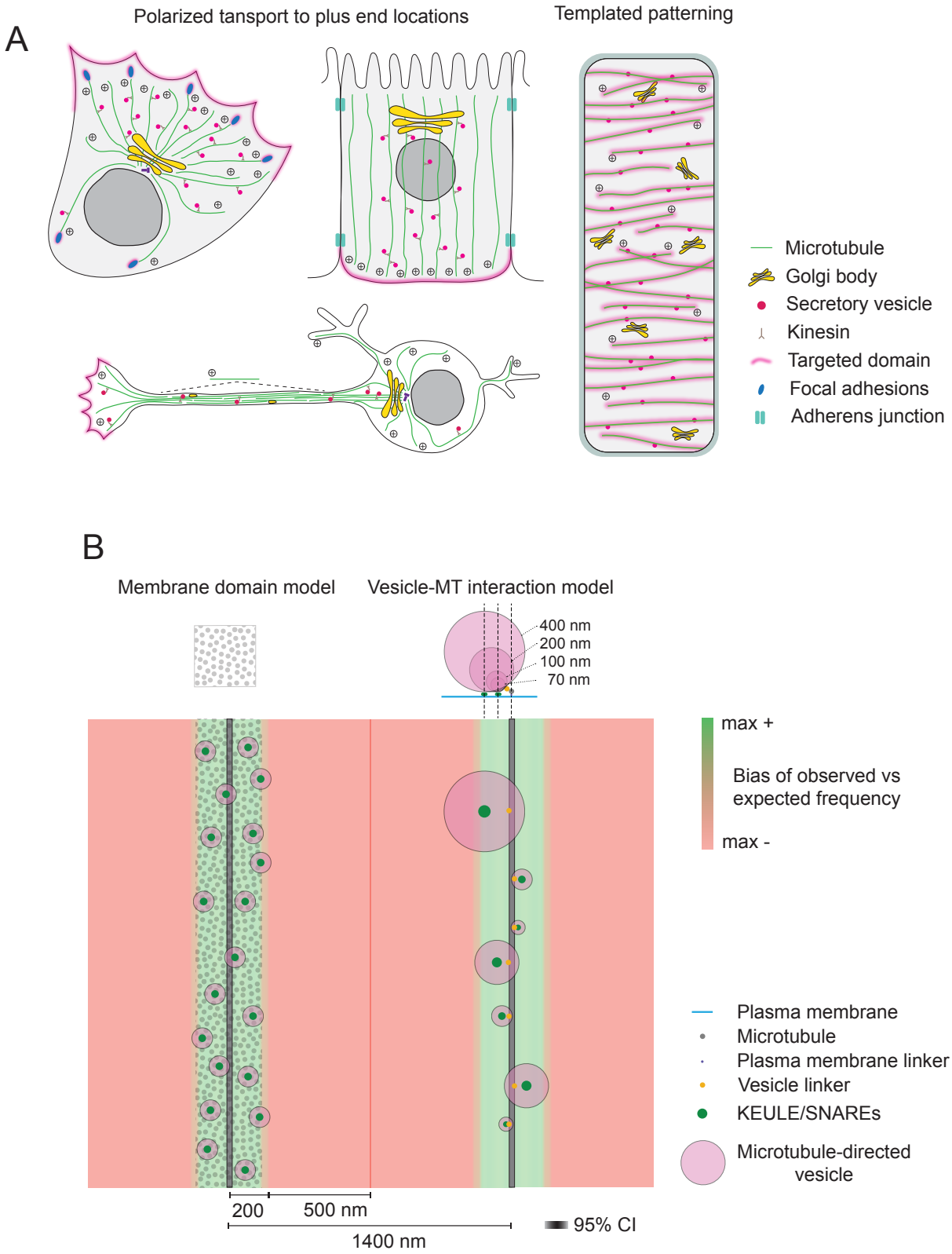

1102

1103 **Fig. 6. Patterning of exocytosis by microtubule arrays. (A)** Schematic diagrams of microtubule-
1104 directed patterning of exocytosis. The three cells on the left show targeting of exocytosis by motor-driven
1105 transport of vesicles along polarized microtubule tracks to locations defined by their plus ends[3] .
1106 Clockwise from upper left: migrating fibroblast, epithelial cell, neuronal cell. By contrast, the diagram at
1107 far right shows an epidermal cell in the plant axis, where a 2-D array of microtubules at the cell cortex
1108 acts as a template that directs exocytosis in a complex but ordered pattern. The organization of the
1109 microtubule lattices defines this pattern. **(B)** Alternative models for spatial patterning of exocytosis by
1110 cortical microtubule arrays in plant cells. All structures are abstracted but depicted at approximate scale.
1111 Microtubules (grey) are shown spaced at the mean spacing that has been measured in the cortical arrays
1112 of growing cells in the hypocotyl epidermis of dark grown *Arabidopsis* seedings[61]. The likelihood of
1113 exocytosis marked by dynamic KEULE clusters is shown as a red-green heat map as scaled from the
1114 observed over-representation and under-representation of KEULE clusters compared to that expected
1115 from the null hypothesis of a random distribution (depicted in Fig. 5B). The two sides of the diagram
1116 depict alternative models to explain the measured spatial dimensions of the domains enriched in
1117 exocytosis. On the right, the measured extent of the enriched domain is determined by the interaction
1118 exocytotic vesicle with microtubules, where those vesicles have a wide range of sizes. On the left,
1119 microtubules establish a membrane domain that extends approximately 180 nm on either side where
1120 proteins needed for vesicle capture or exocytosis are concentrated. These models are not mutually
1121 exclusive. The grey-scale bar at lower right depicts the mean 95% confidence interval for the measured
1122 distances of KEULE clusters to microtubule centers.
1123

1124 **Supplemental Materials**

1125 **Figure S1**

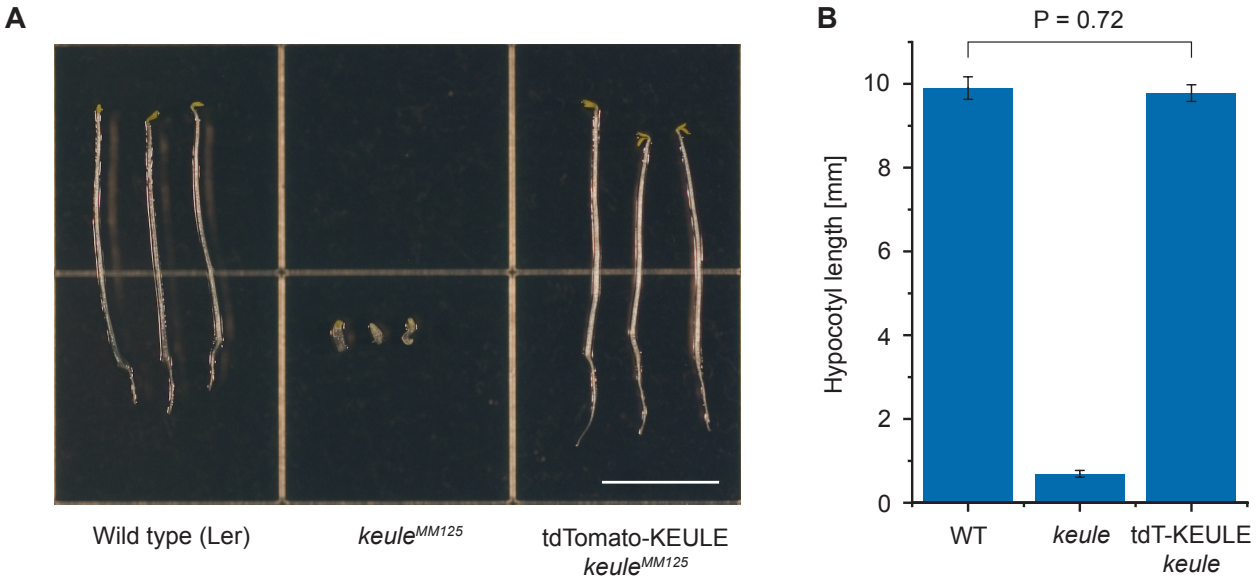

1126

1127 **Fig. S1. Complementation of the *keule* mutation. (A)** Seedlings of indicated genotypes were grown in
1128 the dark for 5 d. The recessive *keule* MM125 allele is seedling lethal; mutant seedlings have bloated,
1129 multinucleate cells. Expression of a tdTomato-tagged version of KEULE, expressed under the control of
1130 the native upstream regulatory element, complemented the *keule* mutation in dark-grown seedlings. Scale
1131 bar, 5 mm. **(B)** Hypocotyl elongation in 5-day-old dark-grown seedlings. Rescued seedlings were
1132 comparable to wild-type (n = 50 plants per genotype, P = 0.72 by t-test). Error bars represent SEM.

1133 **Figure S2**

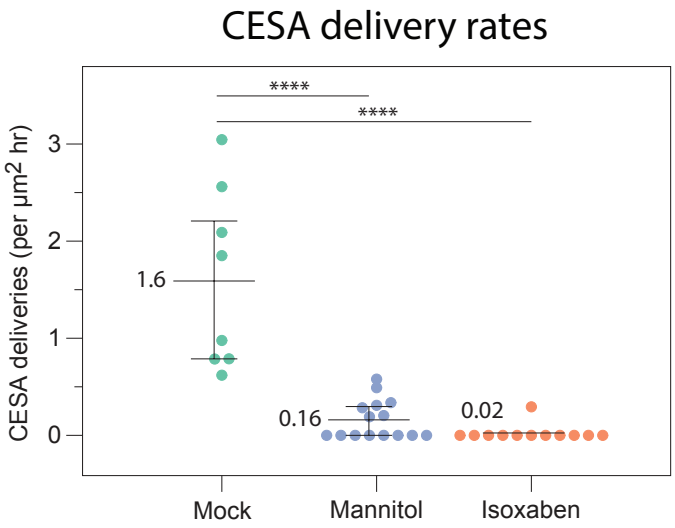

1134

1135 **Fig. S2. CSC delivery rates.** CSC delivery rates to the plasma membrane of cells expressing tdTomato-
1136 KEULE and CIT-CESA6 after treatment with 0.01% DMSO (mock), 200 mM mannitol or 100 nM
1137 isoxaben. See Methods for treatment durations. Values are means, whiskers are quartiles. Mock: n = 8
1138 cells from 8 seedlings, 208 delivery events observed in 1570 μm^2 total area over 0.0828 hr. Mannitol: n =
1139 15 cells from 15 seedlings, 11 delivery events observed in 880 μm^2 total area over 0.0793 hr. Isoxaben: n
1140 = 12 cells from 12 seedlings, 2 delivery events observed in 996 μm^2 total area over 0.0793 hr. ****
1141 $p<0.0001$, Wilcoxon two sample test.

1142 **Figure S3**

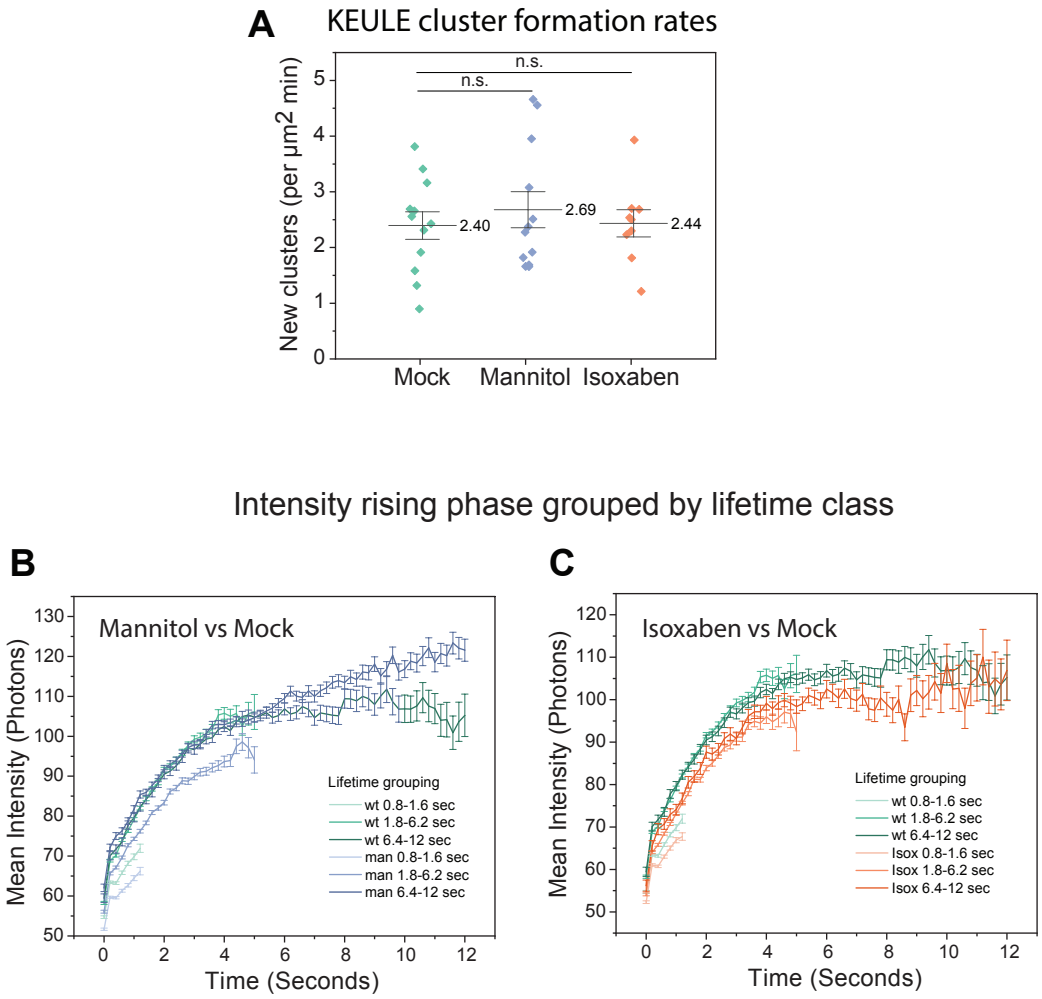

1143
1144

1145 **Fig. S3. Intensity of dynamics of tdTomato-KEULE clusters by lifetime.** (**A**) Average tdTomato-
1146 KEULE cluster signal intensity with lifetimes ranging from 0.8 to 6.8 s for mock, mannitol treatment. and
1147 isoxaben treatment. Whiskers are means and quartiles. n.s. p>0.05 Wilcoxon two sample test. (**B** and **C**)
1148 Comparison of average signal intensities of tdTomato-KEULE clusters in three cumulative lifetime
1149 ranges, 0.8 to 1.6 s, 1.8 to 6.2 s and 6.4 to 12.2 s, between (**B**) mock vs mannitol treatment, and (**C**) mock
1150 vs isoxaben treatment. Mock: n = 15,130 clusters observed in 12 cells from 12 plants. Mannitol: n =
1151 35,496 clusters observed in 15 cells from 15 plants. Isoxaben: n = 25,251 clusters observed in 12 cells
1152 from 12 plants. Error bars are SEM.
1153

1154 **Figure S4**

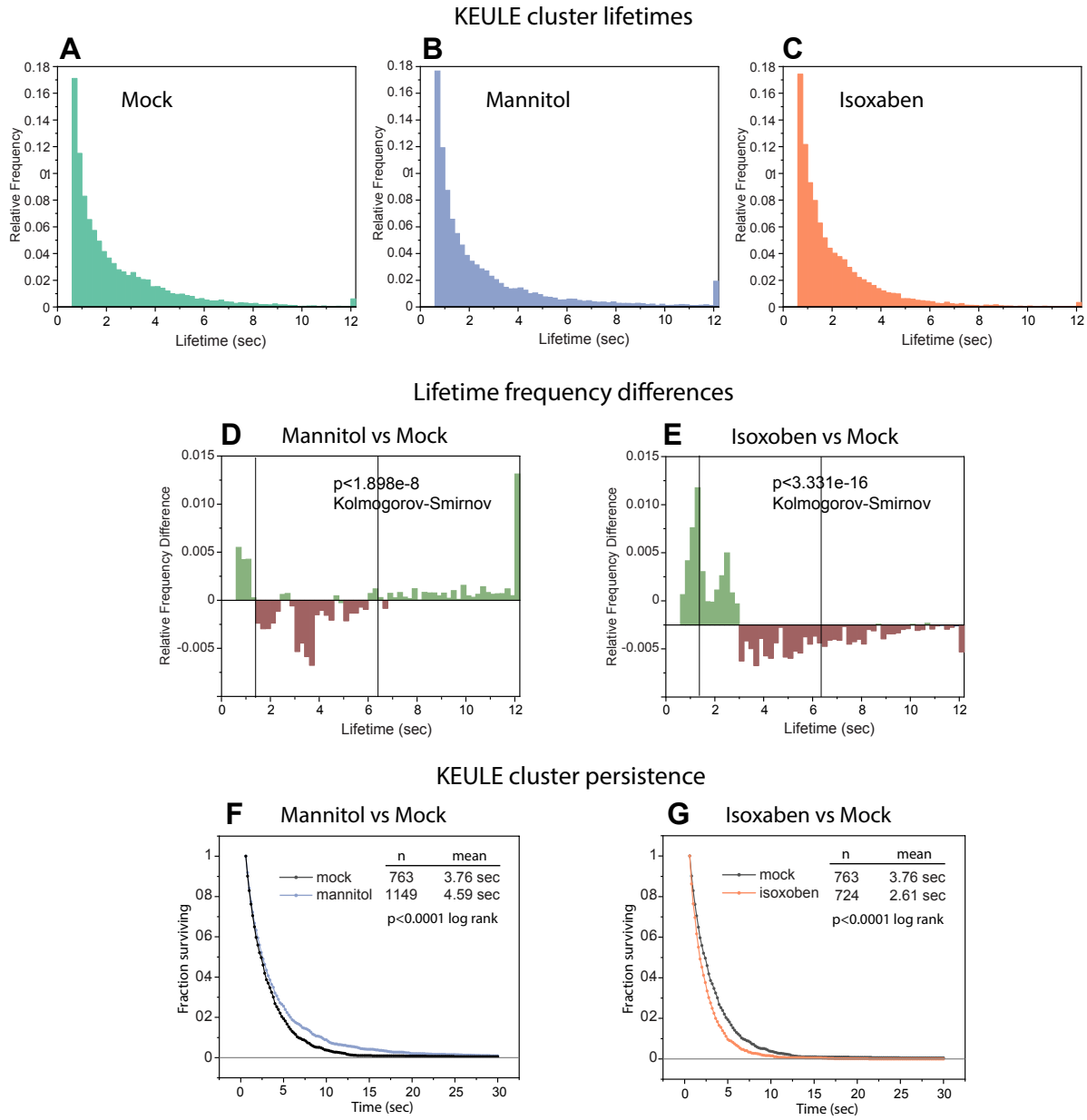

1155

1156 **Fig. S4. KEULE cluster lifetimes.** (**A** to **C**) Lifetime distribution of tdTomato-KEULE clusters in mock
1157 (**A**), mannitol (**B**) and isoxaben (**C**) treated cells. (**D** and **E**) Difference in relative lifetime frequency
1158 between mannitol and mock (**D**), and isoxaben and mock (**E**). Vertical lines indicate the lifetime classes
1159 in Figure 1G. (**F**) Formation rates of new tdTomato-KEULE clusters. Values are means. (**G** and **H**)
1160 Comparison of the fraction of remaining tdTomato-KEULE clusters that were present in the first frame of
1161 the movie for mannitol to mock (**G**) and isoxaben to mock. Mock: n = 763 clusters observed in 12 cells
1162 from 12 plants. Mannitol: n = 1149 clusters observed in 15 cells from 15 plants. Isoxaben: n = 724
1163 clusters observed in 12 cells from 12 plants.

1164

Figure S5

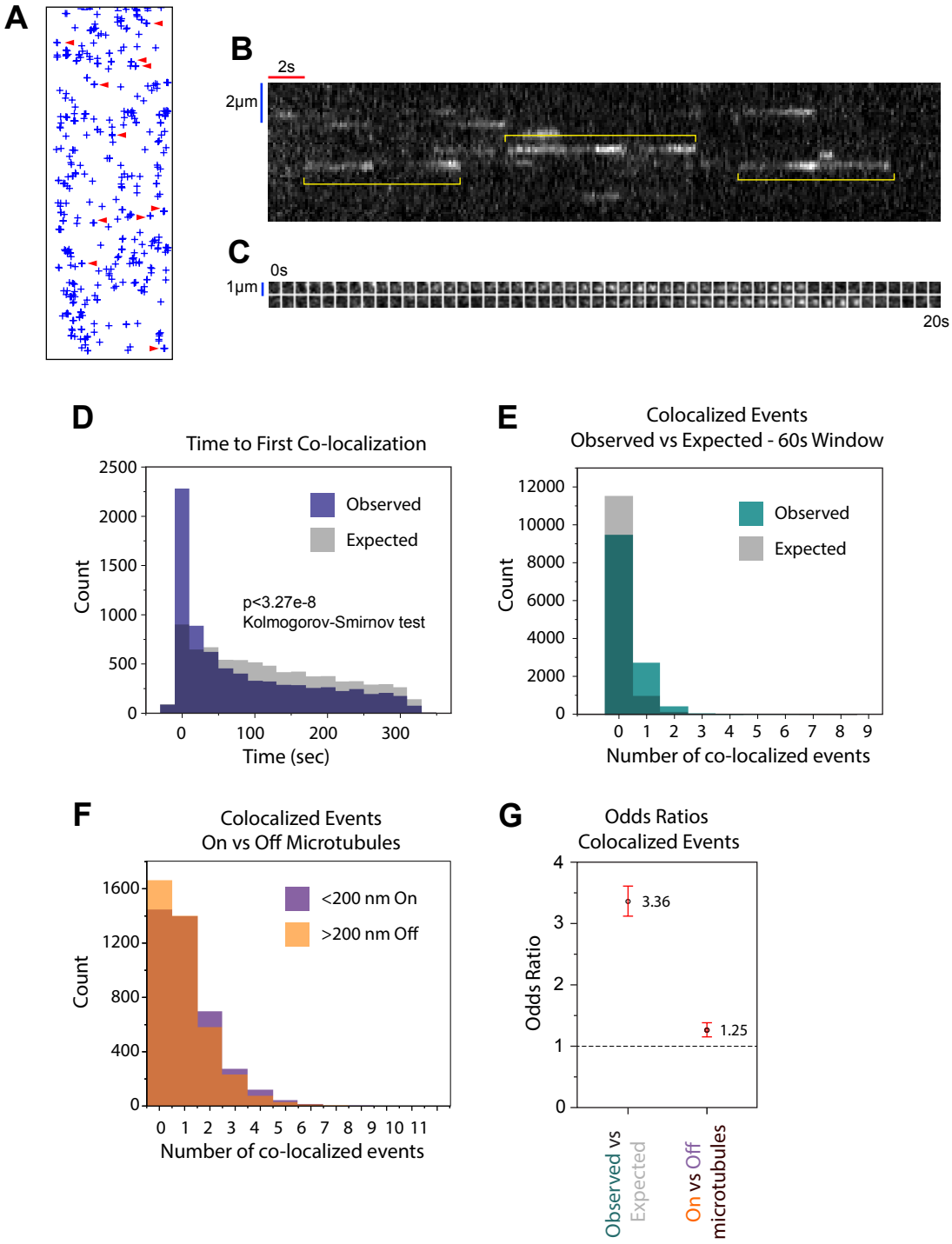
A
B
2s
2μm
C
0s
1μm
20s
D
Time to First Co-localization
Observed
Expected
p<3.27e-8
Kolmogorov-Smirnov test
Count
Time (sec)
E
Colocalized Events
Observed vs Expected - 60s Window
Observed
Expected
Count
Number of co-localized events
F
Colocalized Events
On vs Off Microtubules
<200 nm On
>200 nm Off
Count
Number of co-localized events
G
Odds Ratios
Colocalized Events
Odds Ratio
3.36
1.25
Observed vs Expected
On vs Off microtubules

Fig. S5 KEULE cluster hot spots. (**A**) Map of tdTomato-KEULE cluster detections over x minutes. Crosses are positions determined by MLEwG fitting. Arrowheads indicate examples of repeat detects at the same location, or hot spots. (**B**) Kymograph of tdTomato-KEULE signal along a 3 pixel wide transect line. Yellow brackets indicate examples of repeated KEULE cluster formation at the same location. (**C**) Individual image frames at a hot spot, 200 msec intervals over 20 seconds. (**D**) Distributions of waiting times for a second cluster to appear at the same location as a previous cluster, as defined by a stringent co-localization cutoff distance of 133 nanometers. The distributions for observed data and randomly simulated data are shown in purple and grey, respectively. Note that the observed intervals are significantly skewed to shorter intervals as compared to those in the simulated data ($p<3.27E-8$ Kolmogorov-Smirnov test). n = 12,719 clusters in 17 cells from 17 plants. (**E**) Distributions of the number of co-localized events observed at each KEULE cluster location within 60 seconds of the formation of the first cluster. Colocalization events were 3.36 more frequent in observed data (green) than expected by chance alone (grey), as determined by odds ratio analysis (see panel (**G**)). n = 9458 clusters in 17 cells from 17 plants. (F) Distributions of KEULE colocalization events either on or off microtubules on observed data. The distance threshold for microtubule association was < 200 nm. Sequential KEULE cluster co-localization was 1.25 times more frequent for KEULE events associated with microtubules than for those not associated with microtubules, as determined by odds ratio analysis (see panel (G)). n = 4000 clusters on microtubules and 4866 clusters off microtubules in 17 cells from 17 plants. (G) Odds ratios and 95% confidence intervals for the data shown in panels (G) and (F). The dotted line indicates the odds ratio expected for the null hypothesis of no different from random.

1190

1191 **Figure S6**

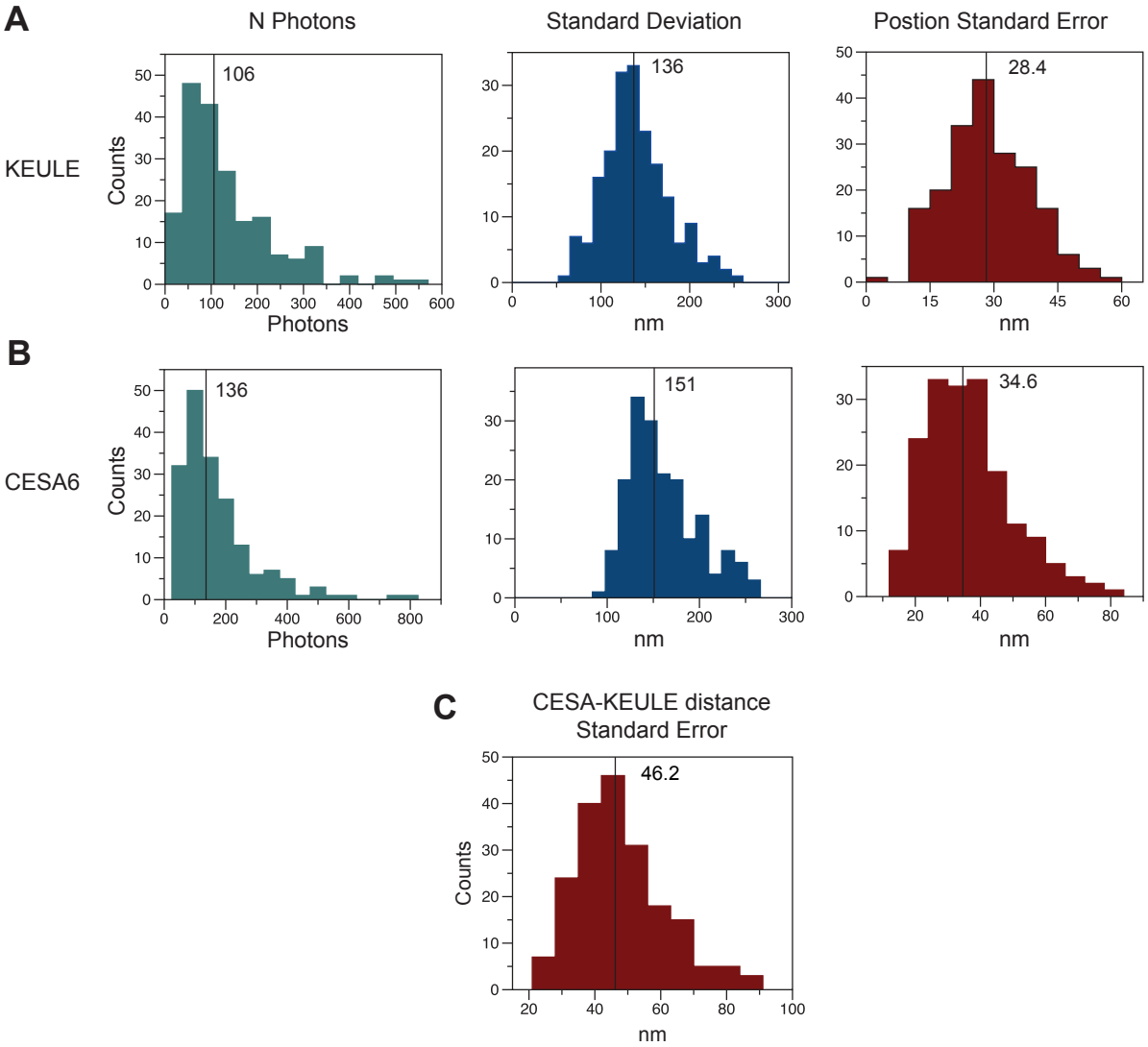

1192

1193 **Fig. S6. Fit parameters for CSC vesicles in the tethering frame and the nearest KEULE clusters to**
1194 **these tethering sites.** (**A**) Distributions of fit parameters for MLEwG fits of tdTomato-KEULE clusters.
1195 (**B**) Distributions of fit parameters for MLEwG fits of CIT-CESA6 signal. (**C**) Distribution of standard
1196 errors for KEULE to microtubule distance measurements. Black lines and values indicate means. n = 194

1197

1198 **Figure S7**

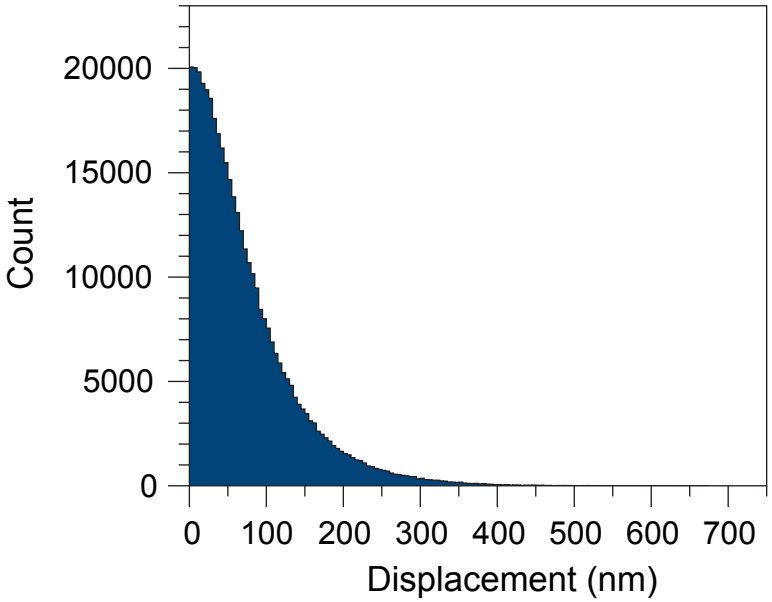

1199

1200 **Fig. S7.** Frame-to-frame displacements of tdTomato-KEULE clusters in 200 ms streaming acquisitions. n
1201 = 283,127 displacements for 15,130 clusters observed in 12 cells from 12 plants.

1202
1203

1204 **Figure S8**

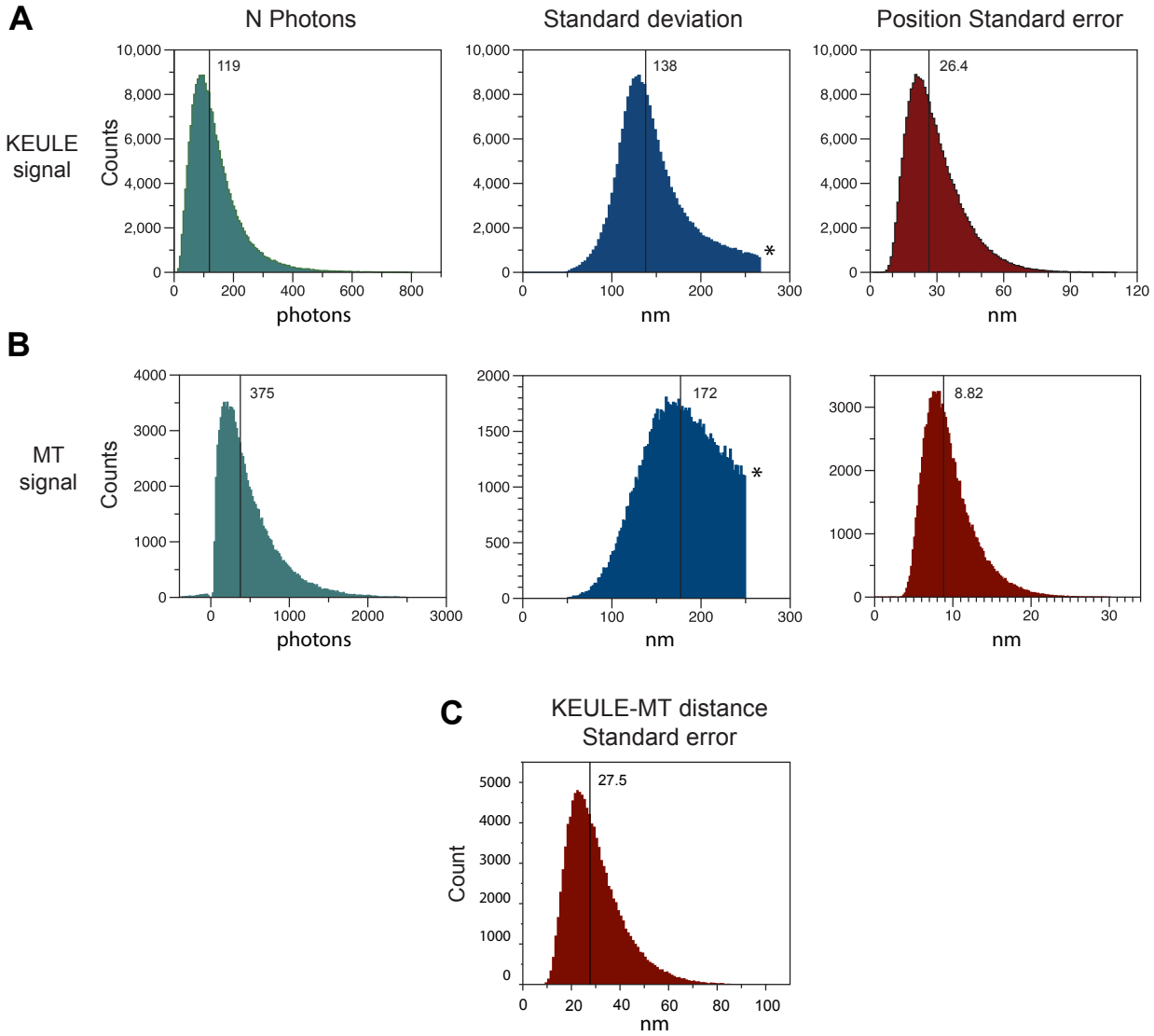

1205

1206 **Fig. S8. Fit parameters for KEULE to microtubule distances used for localization analysis.** (**A**) Fit
1207 parameters for MLEwG fits of tdTomato-KEULE clusters. (**B**) Fit parameters for MLEw1dG fitting of
1208 microtubule signal. (**C**) Standard error of KEULE to microtubule distance measurements. Black lines and
1209 values indicate means. *Truncations of standard deviation distributions are due to cutoff values used to
1210 filter and exclude bad fits due to signal patterns that complicate localization analysis. Bad fits for
1211 tdTomato-KEULE signal occur where more than one tdTomato-KEULE cluster are close in proximity,
1212 and bad fits for microtubule signal occur where microtubules are dense and where they intersect in
1213 complex patterns. n = 115,963 KEULE clusters, nearest microtubule locations and KEULE-microtubule
1214 distances observed in 14 cells from 14 plants.

1215 **Movie S1.**

1216 **tdTomato-KEULE cluster dynamics.** Spinning disk confocal images of tdTomato cluster formation and
1217 loss at the plasma membrane of an epidermal hypocotyl cell in a dark grown *Arabidopsis* seedling. To
1218 reduce noise, images were averaged with a running 3-frame window. Streaming acquisition at 5
1219 frames/sec. Playback at 4x real time.

1220 **Movie S2.**

1221 **MLE Gaussian fits of tdTomato-KEULE clusters.** Spinning disk confocal images of tdTomato-
1222 KEULE clusters in an epidermal hypocotyl cell of a dark grown *Arabidopsis* seedling. Magenta circles
1223 indicate an automated detection of a KEULE cluster. For each of these detects the coordinates of the
1224 signal centroid number of detected photons were estimated by MLE Gaussian fitting (see methods).
1225 Streaming acquisition at 5 frames/sec. Playback at 10x real time.
1226

1227 **Movie S3.**

1228 **KEULE localization to CSC delivery events.** Spinning disk confocal images of co-expressed tdTomato-
1229 KEULE and Cit-CESA6. Filled arrowheads point to locations of tracked CSC signal. Empty arrowheads
1230 point to co-localized KEULE clusters that appear shortly after appearance and positional stabilization of
1231 CESA6 signal. 2 second acquisition intervals. 3-frame running average. Playback at 10x real time.
1232

1233 **Movie S4.**

1234 **MLE Gaussian fits of tdTomato-KEULE clusters and EGFP-TUA5 labeled microtubules.** Spinning
1235 disk confocal images of co-expressed tdTomato-KEULE and EGFP-TUA5 labeled microtubules. White
1236 circles indicate automated KEULE signal detects. The position of each cluster at the first frame of
1237 stabilization was estimated at a sub-pixel level if MLE Gaussian fitting. 1 second acquisition intervals.
1238 Playback at 20x real time.